The cGAS-STING Pathway Affects Vertebral Bone but Does Not Promote Intervertebral Disc Cell Senescence or Degeneration

Olivia K. Ottone [1,2], C. James Kim [1], John A. Collins [1] and Makarand V. Risbud [1,2*]

[1] Department of Orthopaedic Surgery, Sidney Kimmel Medical College, Thomas Jefferson University, Philadelphia, PA, United States,
[2] Graduate Program in Cell Biology and Regenerative Medicine, Jefferson College of Life Sciences, Thomas Jefferson University, Philadelphia, PA, United States

The DNA-sensing cGAS-STING pathway promotes the senescence-associated secretory phenotype (SASP) and mediates type-I interferon inflammatory responses to foreign viral and bacterial DNA as well as self-DNA. Studies of the intervertebral disc in humans and mice demonstrate associations between aging, increased cell senescence, and disc degeneration. Herein we assessed the role of STING in SASP promotion in STING gain-(N153S) and loss-of-function mouse models. N153S mice evidenced elevated circulating levels of proinflammatory markers including IL-1β, IL-6, and TNF-α, showed elevated monocyte and macrophage abundance in the vertebral marrow, and exhibited a mild trabecular and cortical bone phenotype in caudal vertebrae. Interestingly, despite systemic inflammation, the structural integrity of the disc and knee articular joint remained intact, and cells did not show a loss of their phenotype or elevated SASP. Transcriptomic analysis of N153S tissues demonstrated an upregulated immune response by disc cells, which did not closely resemble inflammatory changes in human tissues. Interestingly, STING$^{-/-}$ mice also showed a mild vertebral bone phenotype, but the absence of STING did not reduce the abundance of SASP markers or improve the age-associated disc phenotype. Overall, the analyses of N153S and STING$^{-/-}$ mice suggest that the cGAS-STING pathway is not a major contributor to SASP induction and consequent disc aging and degeneration but may play a minor role in the maintenance of trabecular bone in the vertebrae. This work contributes to a growing body of work demonstrating that systemic inflammation is not a key driver of disc degeneration.

Keywords: Intervertebral disc, cGAS-STING, SASP, aging, nucleus pulposus, inflammation, vertebrae, senescence

INTRODUCTION

Intervertebral disc degeneration is widely accepted as a major risk factor for chronic low back pain and neck pain, two of the leading causes of years lived with disability worldwide (1, 2). The pervasive nature of these pathologies drives the need to understand the underlying mechanisms of major risk factors like disc degeneration. The disc constitutes the largest avascular, and therefore hypoxic,

tissue in the body, and cellular function is tightly governed by the transcription factor HIF-1α (3–7). The disc is comprised of three compartments: an inner, glycosaminoglycan (GAG)-rich nucleus pulposus (NP); a fibrocartilaginous annulus fibrosus (AF), consisting of concentric collagen-rich lamellae surrounding the NP; and inferior and superior cartilaginous endplates (EP), which anchor the disc to adjacent vertebrae and facilitate nutrient diffusion between the vascularized vertebrae and the avascular disc (8). During aging and degeneration, water-imbibing proteoglycans are lost in the NP, and cells undergo morphologic and phenotypic changes, contributing to fibrotic remodeling in the NP and AF compartments and a reduced ability to accommodate spinal loading (9, 10).

A widely recognized risk factor for disc degeneration, a slow progressing pathology, is aging (11). An important contributing factor to age-associated degeneration in the disc and knee joint articular cartilage is cell senescence. In human tissues, the incidence of senescence increases as these tissues age and during degeneration, marked by characteristic SA-β-gal staining, telomere shortening, and elevated P16^{INK4A} expression (12–15). The Ercc1$^{-/Δ}$ progeria mouse model demonstrates genotoxic stress-induced premature senescence and disc degeneration (16, 17). Senescence is of particular interest in degenerative disorders because of the senescence-associated secretory phenotype (SASP) developed by senescent cells. Characteristic of SASP is the secretion of various inflammatory cytokines and proteases – including known markers of disc degeneration IL-6, IL-1, MCP-1, and MMP-1, 3 and 13 – which contribute to the catabolism within tissues and propagate SASP (18, 19). Targeting of senescent disc cells with the senotherapeutic o-vanillin has shown efficacy in reducing SASP *in vitro*, and most recently, the combination senolytic drug treatment of Dasatinib and Quercetin reduced SASP and incidence of disc degeneration *in vivo*, in aged C57B6 mice (20, 21). These studies strongly support the need to further explore and understand the underlying mechanisms which drive disc cell senescence.

One such mechanism which has been demonstrated to promote SASP is the cGAS-STING DNA-sensing pathway which mediates type-I interferon inflammatory responses to foreign, viral, and bacterial DNA as well as self-DNA (22). It has been shown that cellular senescence destabilizes the nuclear membrane, resulting in the release of cytosolic chromatin fragments and consequent activation of the cGAS-STING pathway (23, 24). Notably, *Sting*-null mice show signs of attenuated SASP after exposure to ionizing irradiation, indicating the cGAS-STING pathway is a critical mediator of DNA damage-associated SASP (24). STING has also been implicated in mediating inflammatory processes in musculoskeletal tissues. Deletion of STING in *DNase*$^{+/-}$; *Ifnar*$^{-/-}$ double knockout (DKO) mice – an inflammatory model used to study rheumatoid arthritis – effectively ameliorated paw inflammation and abnormal bone accrual in the long bones and spleens of the DKO animals (25, 26). Recently, a rat model of vertebral inflammation-induced intervertebral disc degeneration, where lipopolysaccharide (LPS) was introduced into vertebral defects, showed a degenerative phenotype marked by

cartilaginous endplate defects, immune cell infiltration, and higher levels of cGAS, STING, TBK1, and IRF3 (27). Likewise, an acute injury model of disc herniation was used by Zhang *et al.* to show that inhibition of STING results in the partial rescue of a degenerative phenotype by modulating NLRP3 signaling (28).

Based on these relationships between disc degeneration, senescence, and STING, we first investigated if, in the absence of a traumatic mechanical injury, activation of STING in the intervertebral disc would promote SASP and a degenerative phenotype and secondly whether the absence of STING would be protective to the intervertebral disc by delaying the SASP program and reducing the prevalence of age-related degeneration in mice. This was achieved by evaluating the spines of mice heterozygous (N153S) for the Sting^{1em1Jmin} mutation that constitutively activates STING without altering STING expression levels and STING$^{-\backslash-}$ mice to assess the contribution of STING to SASP onset and intervertebral disc degeneration (24, 29). Interestingly, neither model demonstrated significant changes in the disc phenotype, with analyses of N153S mice serving as additional support to an emerging concept that when the structural integrity of the disc remains intact, the NP compartment is isolated from systemic inflammation (30). Overall, the analyses of the vertebral columns of N153S and STING$^{-/-}$ mice indicate that the cGAS-STING pathway is not a major contributor to SASP induction and disc degeneration but may play a small role in the maintenance of trabecular bone in the vertebrae.

MATERIALS AND METHODS

Animals
Animals procedures were performed under approved protocols by the IACUC of either Thomas Jefferson University (WT, N153S) or the University of Pennsylvania (STING$^{+/+}$, STING$^{-/-}$). Wildtype (WT) and heterozygous B6J.B6N-*Sting1*^{em1Jmin} (Stock # 033543) knock-in mice with a N153S substitution in the *sting1* gene were obtained from the Jackson Laboratory and aged to 6 months–of–age. WT and N153S animals were collected at 6 months-of-age due to poor survival in N153S mice by one year, resulting from multiple pathologies including progressive lung and perivascular inflammation and T cell cytopenia (29, 31). Tissues from female and male animals were evaluated for evidence of accelerated disc degeneration, osteoarthritis, and SASP. Spines of 16-18 month-old STING$^{+/+}$ and STING$^{-/-}$ mice on a C57BL/6 were provided by Dr. Shelley Berger from the University of Pennsylvania (24, 32). For each genotype, tissues from female and male animals between 16 and 18 months–of–age were evaluated for evidence of delayed age- and senescence-related degeneration.

Plasma Collection and Analysis
Blood from 6-month-old WT (n = 9) and N153S (n = 9) mice was collected immediately postmortem by intracardiac puncture using heparinized needles. Plasma was separated from red blood cells *via* centrifugation at 1500 rcf and 4°C for 15 minutes and stored at -80°C until the time of analysis. Cytokine

concentrations were evaluated using the V-PLEX Mouse Cytokine 19-Plex Kit (Meso Scale Diagnostics, Rockville, MD) according to the manufacturer's specifications.

Micro-Computed Tomography (μCT) Analysis

μCT scans (Bruker Skyscan 1275; Bruker, Kontich, Belgium) were performed on spines from all genotypes (n=6-7 mice/genotype) fixed with 4% PFA. An aluminum filter was used, and all scans were conducted at 50 kV and 200 μA, with an exposure time of 85 ms, yielding a resolution of 15 mm. Three-dimensional image reconstructions were generated from lumbar (L3-L6: WT, N153S; L4-L6: STING$^{+/+}$ STING$^{-/-}$) and caudal (Ca5-Ca9: WT, N153S; Ca5-Ca7: STING$^{+/+}$ STING$^{-/-}$) scans in CTan (Bruker) and used for all subsequent analyses. Intervertebral disc height and vertebral length were measured and used to calculate the disc height index (DHI), as previously described (33, 34). The 3-D microarchitecture of the trabecular bone was tabulated in a region of interest (ROI) defined by contouring the outer boundary of the trabeculae throughout the vertebral body. Resulting datasets were assessed for the following parameters: structure model index (SMI), bone volume fraction (BV/TV), trabecular number (Tb. N.), trabecular thickness (Tb. Th.), and trabecular separation (Tb. Sp.). The cortical bone was analyzed in two dimensions and assessed for bone volume (BV), cross sectional thickness, mean cross-sectional bone area, and bone perimeter. Mineral density was calculated in lumbar vertebrae and boney endplates using a standard curve created with a mineral density calibration phantom pair (0.25 g/cm3 calcium hydroxyapatite (CaHA), 0.75 g/cm3 CaHA).

The hindlimbs of WT and N153S (n=2 limbs/animal, 3 animals/genotype, 6 limbs/genotype) were scanned using an aluminum filter at 70 kV and 142 μA, with an exposure time of 55 ms, yielding a resolution of 7 μm. 3-D analysis as described above was conducted on the knee joints, and BV/TV, Tb. Th., Tb. Sp., and the subchondral bone plate thickness (SCBP Th.) were assessed between genotypes.

Biomechanical Analysis

Caudal vertebrae (Ca2-4) from 6-month-old WT and N153S mice (n=12 animals/genotype) were isolated and stored in PBS-soaked gauze at -80°C before use. Samples underwent two freeze-thaw cycles and were scanned using μCT prior to testing. Each vertebra was individually potted into a 2-mm plastic ring mold using an acrylic resin (Ortho-Jet, Patterson Dental, Saint Paul, MN), and mechanical loading was applied using a material testing system (TA Systems Electrofoce 3200 Series II). A 0.4-N compressive preload was applied, followed by a monotonic displacement ramp at 0.1 mm/s until failure. Force-displacement data were digitally captured at 25 Hz and converted to stress-strain using a custom GNU Octave script with μCT-based geometric measurements, as previously described (35, 36).

Histological Analysis

Spine segments used for calcified sections (WT and N153S: L1-L2, Ca1-Ca2) were fixed for 2 hours in 4% PFA in PBS, treated with 30% sucrose, OCT-embedded, and snap-frozen. For all genotypes, caudal and lumbar spines were dissected and immediately fixed in 4% PFA in PBS at 4°C for 48 hours. 18 days of decalcification in 20% EDTA at 4°C followed, and spines were then embedded in paraffin. Coronal sections of 7 μm were generated from caudal (Ca5-Ca9: WT, N153S; Ca3-Ca7: STING$^{+/+}$ STING$^{-/-}$) and lumbar (L3-LS1: WT, N153S; L1-S1: STING$^{+/+}$ STING$^{-/-}$) discs. Histoclear deparaffinization followed by graded ethanol rehydration preceded all staining protocols. Caudal (n=4 discs/mouse, 6-7 mice/genotype) and lumbar (n=4-6 discs/mouse, 6-7 mice/genotype) tissues were stained with Safranin O/Fast Green/Hematoxylin or Picrosirius red and imaged using a light microscope (AxioImager 2; Carl Zeiss Microscopy, Peabody, MA, USA) or a polarizing light microscope (Eclipse LV100 POL; Nikon, Tokyo, Japan). Imaging of Safranin O-stained tissues was performed using 5x/0.15 N-Achroplan and 20x/0,5 EC Plan-Neofluar (Carl Zeiss) objectives and Zen2^{TM} software (Carl Zeiss). Six blinded graders scored NP and AF compartments, using Modified Thompson Grading (37). Picrosirius red-stained tissues were imaged using 4x and 20x 10×/0.25 Pol/WD 7.0 (Nikon) objectives, and the areas occupied by green, yellow, or red pixels were determined using the NIS Elements Viewer software (Nikon).

WT and N153S hindlimbs (n=1 limb/animal, 3 animals/genotype, 3 limbs/genotype) were processed according to the aforementioned fixation and decalcification protocols. 5 μm sections cut in the coronal plane underwent deparaffinized followed by graded ethanol rehydration. Midcoronal sections were stained with toluidine blue or H&E and imaged using a light microscope with 10x objectives (Motic BA300 POL; Motic, Schertz, TX, USA) and Jenoptik ProgRes Speed XT Core 5 camera with the ProgRes Capture Pro software (version 2.10.0.1) (Jenoptik Optical Systems). Histological scoring of cartilage damage, OA severity, osteophyte formation, and chondrocyte cell death was conducted using the ACS scoring system, as previously detailed (38, 39).

TRAP and TNAP Staining

Frozen calcified sections of WT and N153S discs (L1-L2, Ca1-Ca2) were cut at 10 μm and secured to slides using cryofilm 2C (10) to maintain the morphology of the mineralized sections (40). The taped sections were glued to microscope slides using chitosan adhesive and rehydrated prior to imaging. Sections were also stained to detect activity of tartrate-resistant acid phosphatase (TRAP) (1:80, Invitrogen, E6601A) and tissue non-specific alkaline phosphatase (TNAP) (Vector Laboratories, SK5300).

TUNEL Assay and Cell Number Quantification

TUNEL assay was performed on N153S and WT lumbar disc tissue sections using an *in situ cell death detection* kit (Roche Diagnostic). Briefly, sections were deparaffinized and permeabilized with Proteinase K (20 mg/mL) for 15 min at room temperature. The TUNEL assay was then carried out per the manufacturer's protocol. The sections were washed and mounted with Prolong Gold Antifade Mountant with DAPI (Thermo Fisher Scientific, P36934). All mounted slides were imaged with an Axio Imager 2 microscope using 5 x/0.15 N- Achroplan or 10 x/0.3 EC Plan-Neofluar or 20 x/0.5 EC Plan-Neofluar objectives, (Carl Zeiss) X-

CiteÒ120Q Excitation Light Source (Excelitas), AxioCam MRm camera (Carl Zeiss), and Zen2TMsoftware (Carl Zeiss). TUNEL-positive cells and DAPI-positive cells were analyzed respectively to assess cell death and cell number in disc compartments

Immunohistochemical Analysis

All immunohistochemical stains were conducted on mid-coronal lumbar sections of 7μm. Sections were deparaffinized and rehydrated, as described under Histological Analysis. Antibody-specific antigen retrieval was conducted by way of incubation in either a hot citrate buffer for 20 minutes, proteinase K treatment for 7-10 minutes at room temperature, or chondroitinase ABC for 30 minutes at 37°C. Sections were then blocked in 1-5% normal serum (Thermo Fisher Scientific, 10,000C) in PBS-T (0.4% Triton X-100 in PBS), and incubated with primary antibodies against F4/80 (1:100; Cell Signaling; 70076S), MHC II (1:100; Fisher Scientific; 50-112-9377), Ly-6G (1:100; Biolegend; 127602), Aggrecan (1:50; Millipore; AB1031), CA3 (1:150; Santa Cruz Biotechnology; sc-50715), Collagen I (1:100; Abcam; ab34710), IL-6 (1:50; Novus; NB600-1131), TGF-β1 (1:100; Abcam; ab92486), IL-1β (1:100; Novus; NB600-633), p19 (1:100; Novus; NB200-106), p21 (1:100, Novus NB1001941), Collagen IX (1:500; Abcam; ab134568), COMP (1:200; Abcam; ab231977), or Collagen II (1:400; Fitzgerald; 70R-CR008). Tissue sections were washed and incubated with the appropriate Alexa Fluor® -594 or -647 conjugated secondary antibody (1:700; Jackson ImmunoResearch Laboratories, Inc., West Grove, PA, USA) for one hour in the dark at room temperature. Sections were washed again with PBS-T (0.4% Triton X-100 in PBS) and mounted with ProLong® Gold Antifade Mountant with DAPI (Thermo Fisher Scientific; P36934). Mounted disc sections were visualized with Axio Imager 2 (Carl Zeiss Microscopy), using a 10×/0.3 EC Plan-Neofluar (Carl Zeiss Microscopy) objective, X-Cite® 120Q Excitation Light Source (Excelitas Technologies), AxioCam MRm camera (Carl Zeiss Microscopy), and Zen2TM software (Carl Zeiss Microscopy). Exposure settings remained constant across genotypes for each antibody (n=4-6 discs/mouse, 6-7 mice/genotype; n=2 vertebrae/mouse, 6-7 mice/genotype).

Digital Image Analysis

All immunohistochemical quantification was conducted in greyscale using the Fiji package of ImageJ (41). Images were thresholded to create binary images, and NP and AF compartments were manually defined using the Freehand Tool. These defined regions of interest were then analyzed either using the Analyze Particles (TUNEL and cell number quantification) function or the Area Fraction measurement.

Fourier-Transform Infrared Spectroscopy

5-μm deparaffinized sections of decalcified caudal disc tissues were collected from STING$^{+/+}$ and STING$^{-/-}$ mice (n=1 disc/mouse, 4 mice/genotype) and used to acquire infrared (IR) spectral imaging data using methods previously described (10). Briefly, spectra were collected across the mid-IR region of three consecutive sections/disc. Using the ISys Chemical Imaging Analysis software (v. 5.0.0.14) mean second-derivative absorbances in the amide I (1660 cm-1), collagen side chain vibration (1338 cm-1), and proteoglycan sugar ring (1064 cm-1) regions were quantified and compared in the NP, AF, EP, and vertebrae (VB) of STING$^{+/+}$ STING$^{-/-}$ mice. Significant differences in parameters were assessed by t-test or Mann-Whitney test, where relevant, $p < 0.05$ was considered significant.

Spectral Clustering Analysis

Collected spectra were analyzed using K-means clustering analysis in the Eigenvector Solo+MIA software (v. 8.8) to agnostically delineate anatomical regions within the disc, using methods previously reported (10, 42). Briefly, during this analysis, regions of IR images are separated into two or more classes, or "clusters", according to spectral similarity. The K-means partitional clustering method starts with the manually defined selection of K objects that are to be used as cluster targets, where K is determined a priori. During each iteration, the remaining objects (pixels of the spectral image) are assigned to one of these clusters based on the distance from each of the K targets. New cluster targets are then calculated as the means of the objects in each cluster, and the procedure is repeated until no objects are reassigned after the updated mean calculations.

RNA Isolation, Microarray Assay, and Bioinformatic Analysis

NP and AF tissues were separately micro-dissected from WT and N153S animals under a stereo microscope (Zeiss, Stemi 503) and immediately placed in RNAlater® Reagent (Invitrogen, Carlsbad, CA) as previously described (30). For each animal, tissues from L1-S1 and Ca1-Ca15 were pooled to serve as a single sample (n = 20 discs/animal, 5 animals/genotype). NP and AF tissues were homogenized with a Pellet Pestle Motor (Sigma Aldrich, Z359971), and RNA was extracted from the lysates using an RNeasy® Mini kit (Qiagen). Purified DNA-free RNA was quantified, and quality was assessed using a Nanodrop ND 100 spectrophotometer (Thermo Fisher Scientific) and Agilent 2200 TapeStation (Agilent Technologies, Palo Alto, CA, USA) respectively. The GeneChip Pico kit (Thermo Fisher Scientific) was used to synthesize fragmented biotin-labeled cDNA. Mouse Clariom S gene chips were hybridized with fragmented, biotin-labeled cDNA in 100 μL of hybridization cocktail. Arrays were washed and stained with GeneChip hybridization wash and stain kit using GeneChip Fluidics Station 450 (Thermo Fisher Scientific) and subsequently scanned on an Affymetrix GeneChip Scanner 3000 7G, using Command Console Software (Affymetrix, Santa Clara, CA, USA). CHP files were generated by sst-rma normalization from CEL files, and quality control of the experiment was performed in the Transcriptome Analysis Console (TAC) v4.0.2 (Affymetrix). The experimental group was compared to the control group in the TAC, including all probe sets where at least 50% of the samples had a DABG (detected above background) $p < 0.05$. Inclusion cutoffs were defined at a 2.0-fold change and p-value ≤ 0.05. Significantly differentially up- and downregulated genes from the NP and AF compartments were analyzed using the Overrepresentation Test in PANTHER (43, 44).

Human Microarray Data Analysis

Human sample details are as reported by Kazian et al., and data were obtained from GSE70362 in the GEO database (45). Hierarchical clustering comparing DEGs (inclusion cutoffs of p < 0.05 and 2.0-fold change) in degenerative and non-degenerative samples was conducted with a Euclidean distance < 0.05 cut-off. Each degenerated cluster defined was compared to the aggregated non-degenerated cluster, and the up- and downregulated DEGs identified by each comparison were analyzed for GO biological process enrichment using the PANTHER overrepresentation test, FDR ≤ 0.05.

Statistical Analyses

Statistical analysis was performed using Prism 9 (GraphPad, La Jolla, CA, USA) with data presented as mean ± standard deviation (SD), p<0.05. For *in vivo* analyses, data distribution was checked with the Shapiro-Wilk normality test; a Student's t-test was applied to normally distributed data, and a Mann-Whitney test was applied to non-normally distributed data. Distribution data were compared using a x^2 test.

RESULTS

N153S Mice Evidence Elevated Levels of Circulating Proinflammatory Cytokines

To assess the systemic impact of constitutive STING activity, we measured the levels of 19 cytokines and proinflammatory molecules from the plasma of 6-month-old N153S and WT mice using an MSD multiplex assay. N153S mice carry a Sting[1em1Jmin] mutation resulting in the production of constitutively active STING from the endogenous locus without altering the expression level (29). N153S mice showed significant increases in IL-1β (p = 0.0174) (**Figure 1A**), IL-6 (p = 0.0079) (**Figure 1B**), TNF-α (p = 0.0360) (**Figure 1C**), IFN-γ (p = 0.0074) (**Figure 1D**), MIP-1α/CCL3 (p = 0.0025) (**Figure 1E**), IL-2 (p = 0.0152) (**Figure 1F**), and IL-27/p28/IL-30 (p = 0.0016) (**Figure 1G**), MCP-1 (p = 0.0037) (**Figure 1H**), and IP-10 (p = 0.0142) (**Figure 1I**). We did not observe significant changes in plasma levels of IL-33 (**Figure 1J**), IL-5 (**Figure 1K**), IL-10 (**Figure 1L**), IL-15 (**Figure 1M**), MIP-2 (**Figure 1N**), or KC/GRO (**Figure 1O**); whereas IL-4, IL-9, IL-12/p70, and IL-17p28/IL-30 levels were outside of the assay's detection limits. These results suggested systemic hypercytokinemia associated with cGAS-STING activation.

Constitutive STING Activity Compromises Trabecular and Cortical Vertebral Bone Properties But Not Knee Joints

In models of systemic inflammation induced by DNase II and *Ifnar*-inactivation, activation of the STING pathway has been implicated in pathological bone formation (26). STING deficiency in these mice resolved trabecular bone accrual in long bones and spleens, and transcriptomic analysis indicated STING modulates osteoblast activity, bone matrix remodeling, and osteoclast activity (26). While this offers insight into how STING activity may contribute to the regulation of musculoskeletal tissues, its impact on the spinal column remains to be assessed. To understand the impact of constitutive STING activity on the vertebrae, trabecular and cortical bone morphology were analyzed in the lumbar and caudal spines of WT and N153S mice using micro-computed tomography (μCT). The distal femur was also analyzed for its potential impact on articular joint health. Three-dimensional reconstructions of lumbar (**Figures 2A, A'**) and caudal (**Figures 2B, B'**) vertebral motion segments show reductions in the caudal vertebral length (**Figure 2C**), lumbar and caudal disc height (**Figure 2D**), and the lumbar disc height index (DHI) (**Figure 2E**). In the trabecular bone, reductions to the bone volume fraction (BV/TV) (**Figure 2F**) and trabecular thickness (Tb. Th.) (**Figure 2G**) were observed in N153S caudal but not lumbar vertebrae, while trabecular number (Tb. N.) (**Figure 2H**), trabecular spacing (Tb. Sp.) (**Figure 2I**), and structure model index (SMI) (**Figure 2J**) did not vary across genotypes or region of the spine. Similarly, the bone volume (BV) (**Figure 2K**), perimeter (B. Pm.) (**Figure 2L**), and area (B. Ar.) (**Figure 2M**) were lower in the cortical shell of caudal but not lumbar vertebrae of N153S mice, and the cross-sectional thickness (Cs. Th.) was not impacted (**Figure 2N**). Bone mineral density (BMD) was also assessed in the lumbar vertebrae of WT (**Figure 2O**) and N153S (**Figure 2O'**) animals through the vertebral body (**Figure 2P**) and boney endplates (**Figure 2Q**); no differences were observed across genotypes. This was consistent with a lack of differences in TRAP (**Figures 2R, R'**) or TNAP (**Figures 2S, S'**) activity. Moreover, the changes observed in the caudal vertebrae did not translate to altered biomechanics, as indicated by the structural (**Supplementary Figures 1A–D**) and corresponding material properties (**Supplementary Figures 1E–H**). Though ultimate displacement (**Supplementary Figure 1C**) was higher in N153S vertebrae, this change was lost when scaled to geometry, as seen from comparable ultimate strain (**Supplementary Figure 1G**). It is important to note that trends toward a lower ultimate load (**Supplementary Figure 1A**) and higher ultimate stress (**Supplementary Figure 1E**) were due to the smaller size of the N153S vertebrae. This analysis suggests it is unlikely N153S vertebrae manifested any functional consequences of STING activation. In the knees of WT and N153S mice (**Figures 2T, T'**), μCT analysis showed STING activation did not result in osteophyte formation or meniscal ossification. Additionally, 3D analysis of the joint demonstrated comparable BV/TV (**Figure 2U**), Tb. Sp. (**Figure 2V**), Tb. Th. (**Figure 2W**), and subchondral bone plate thickness (SCBP Th.) (**Figure 2X**) between genotypes. Interestingly, N153S vertebrae did evidence elevated levels of MHC II (**Figures 3A, 3A'**), F4/80 (**Figures 3A1, 3A1'**, **B**), and Ly-6G (**Figures 3C-C''**) in the marrow, indicating greater macrophage and monocyte abundance and activation in conjunction with the elevated systemic inflammation. Together, these results demonstrate a region-specific impact of STING activation on the vertebrae and indicate STING activity reduces caudal trabecular and cortical bone structural metrics without significantly affecting bone function.

Intervertebral Discs and Articular Cartilage of N153S Mice Do Not Evidence Accelerated Degeneration

hSTING-N154S transgenic mice show cartilaginous tissue damage, evidenced by paw swelling, tail shortening, and the loss of ear
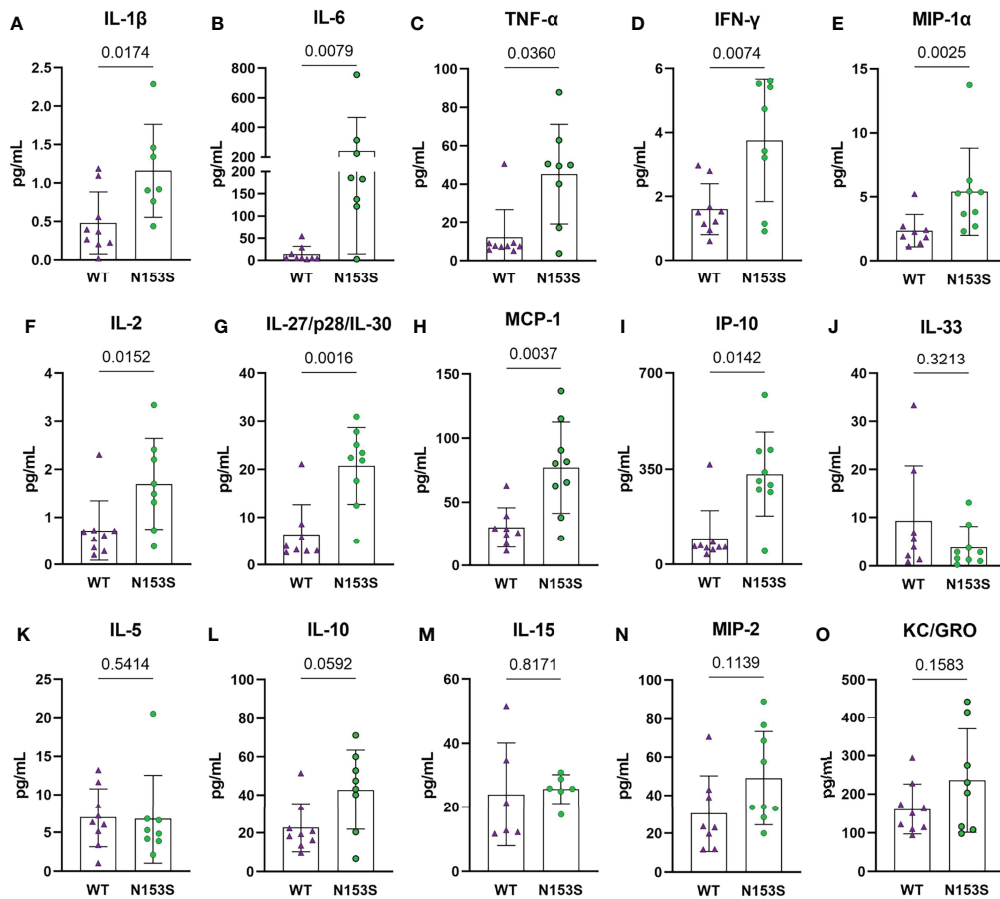
FIGURE 1 | Circulating cytokine levels indicate a proinflammatory environment in N153S mice. Multiplex assay analysis shows a significant increase in the concentrations of **(A)** IL-1β, **(B)** IL-6, **(C)** TNF-α, **(D)** IFN-γ, **(E)** MIP-1α, **(F)** IL-2, **(G)** IL-27/p28/IL-30, **(H)** MCP-1, and **(I)** IP-10 in the plasma of N153S mice. Levels of **(J)** IL-33, **(K)** IL-5, **(L)** IL-10, **(M)** IL-15, **(N)** MIP-2, and **(O)** KC/GRO did not differ between genotypes. Data are shown as mean ± SD. (n = 9 animals/genotype) Significance was determined using an unpaired t-test or Mann-Whitney test, as appropriate.

cartilage (46). Noteworthy, unlike N153S mice, these mice express hN154S, a constitutively active human mutation, through the *Rosa* locus, resulting in elevated STING activity and higher expression levels of hSTING (46, 47). We thereby investigated the histological consequences of constitutive STING activation in the cartilaginous tissues of N153S mice. Safranin O/fast green and hematoxylin staining showed the overall disc tissue architecture was well-preserved in N153S relative to WT mice in lumbar (**Figures 4A, A'**) and caudal (**Figures 4B, B'**) regions. N153S discs were healthy, as demonstrated by aggrecan-rich NP tissue, vacuolated NP cells, well-organized lamellae in the AF, and a uniform layer of hyaline cartilage with discrete cellular organization in the EP. Modified Thompson scores support these observations, demonstrating no differences in the average (**Figure 4D**) NP or AF scores across genotypes in lumbar and caudal regions; however, there were differences in the distribution of lumbar scores and caudal AF scores (**Figure 4C**) (37, 48–51). These differences did not manifest in any level-by-level changes in the average histological scores (**Figures 4E, F'**) and largely do not indicate any trends toward a degenerative phenotype in N153S compared to WT mice. Morphological assessment of the NP

health was affirmed at the molecular level, with immunohistological staining showing comparable abundance of aggrecan (**Figures 4G, G'**) and the NP-phenotypic marker carbonic anhydrase 3 (**Figures 4H, H'**) between N153S and WT mice. Interestingly, despite uncompromised AF morphology, collagen I (**Figures 4I, I'**) abundance was lower in the AF of N153S animals. To determine if apoptosis was accelerated by constitutive STING activity in the disc tissues of N153S animals, TUNEL staining was performed (**Figure 4J**), demonstrating no increase in apoptosis (**Figure 4J'**) and no change in the number of disc cells (**Figure 4J"**) in N153S mice. The articular cartilage health in the knee joint was also assessed with toluidine blue (**Figures 4K, K'**) and H&E (**Figures 4L, L'**) staining, with stains showing no damage to the tissue, cell death, or osteophyte formation in N153S mice. When ACS scoring was conducted by blinded graders, N153S and WT animals all received scores of zero, indicating healthy cartilage (38, 39). Intact disc architecture, overall retention of core structural proteins, and the lack of evidence supporting increased cell death in N153S discs and knee articular cartilage indicate STING activity does not accelerate disc or articular cartilage degeneration.
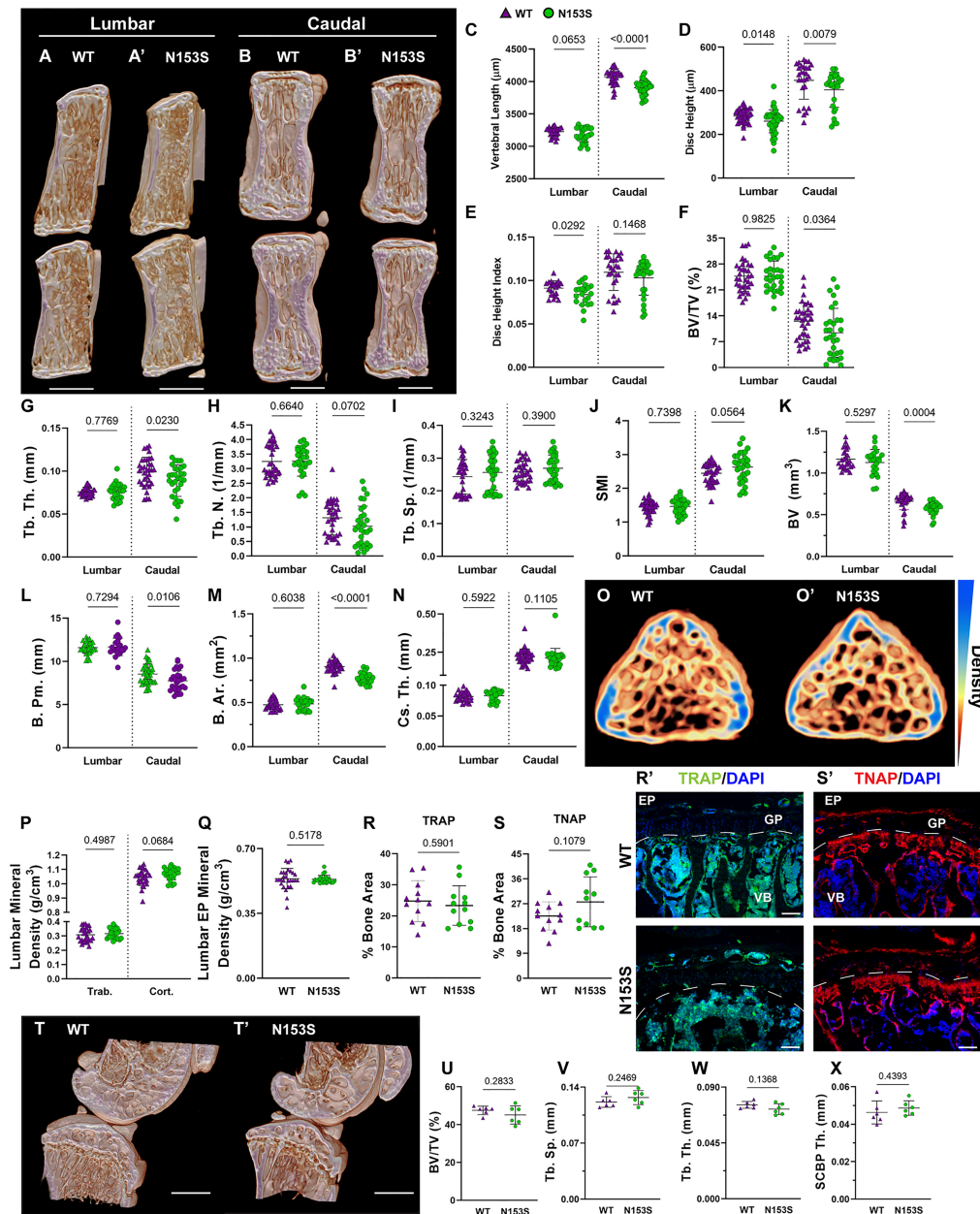
FIGURE 2 | Constitutive STING activity compromises trabecular and cortical vertebral bone properties but not knee joints. (A, B') Representative µCT reconstructions of the hemi-section of a lumbar (A, A') and caudal (B, B') motion segment in a 6-month-old WT and N153S mouse. (C) Vertebral length, (D) disc height, (E) and disc height index (DHI) are shown for lumbar and caudal vertebrae. (F, J) Trabecular bone properties of (F) BV/TV, (G) Tb. Th. (trabecular thickness), (H) Tb. N. (trabecular number), (I) Trab. Sp. (trabecular separation), and (J) SMI (structure model index) are shown for lumbar and caudal vertebrae. (K–N) Cortical bone properties of (K) BV (bone volume), (L) (B) Pm. (bone perimeter), (M), (B) Ar. (bone area), and (N) Cs. Th. (cross-sectional thickness) are shown. (O, O') Representative cross-sections of lumbar WT and N153S vertebral bodies, with mineral density indicated on a yellow (less dense) to blue gradient (more dense). (P) Overall trabecular and cortical mineral density and (Q) bony endplate mineral density are shown. Quantitative immunofluorescence of (R, R') TRAP and (S, S') TNAP activity in the caudal vertebrae. Dotted lines delineate the growth plate (GP) from the rest of the vertebral body (VB). (T, T') Representative µCT reconstructions of the medial femoral condyle and tibial plateau. (U) BV/TV, (V) trabecular separation (Tb. Sp.), (W) trabecular thickness (Tb. Th.), and (X) the subchondral bone plate thickness (SCBP Th.) in the hind joints demonstrate no deviations in N153S mice. (n = 2 joints/animal, 3 animals/genotype, 6 joints/genotype) Quantitative measurements represent mean ± SD (n = 6 lumbar discs and 4 vertebrae/mouse, 7 mice/genotype; n = 4 caudal discs and 5 vertebrae/mouse, 7 mice/genotype). (A, B') Scale bar = 1mm. (O, O') Scale bar = 250 µm. Significance was determined using an unpaired t-test or Mann-Whitney test, as appropriate.
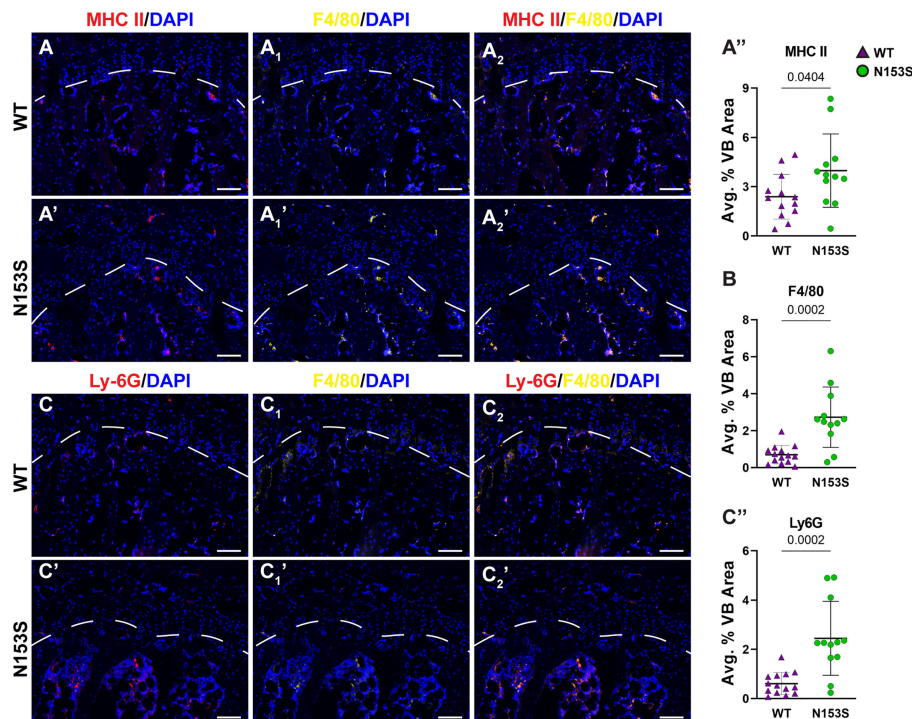
FIGURE 3 | N153S vertebrae show increases in macrophages and monocytes. Immunohistological staining conducted on 6-month-old WT and N153S vertebrae for **(A, A')** MHC II co-stained with **(A₁, A₁')** F4/80 and their **(A₂, A₂')** overlap, with each stain **(A", B)** individually quantified. Quantitative staining was also conducted for **(C-C")** Ly-6G co-stained with F4/80. Images were taken at 10x (scale bar=100 μm). (n = 6-7 animals/genotype, 2 vertebrae/animal, 12-14 total vertebrae/genotype) Dotted lines demarcate different the boundary of the vertebral growth plate. Quantitative data represents the mean ± SD. Significance was determined using unpaired t-test.

SASP Induction Is Not Accelerated in the Discs of N153S Mice

Though the N153S discs did not evidence signs of degeneration, it remained possible for molecular changes to manifest prior to a morphological phenotype or without impacting the disc compartment morphology (19). To assess if this was the case for SASP induction, we conducted immunohistological staining. While levels of IL-6 were elevated (**Figures 5A, A'**) in the NP of N153S mice, compared to WT animals. TGF-β (**Figures 5B, B'**) and IL-1β (**Figures 5C, C'**) levels were unchanged across genotypes. Moreover, abundance of p19 (**Figures 5D, D'**) and p21 (**Figures 5E, E'**) remained unaffected in N153S mice, indicating STING activation does not impact the overall onset of cellular senescence or SASP induction.

## STING Activation Results in More Prominent Transcriptomic Changes in the AF Than the NP of N153S Mice

Microarray analysis was conducted on NP and AF tissues collected from WT and N153S mice to gain insights into transcript-level changes caused by constitutive STING activation. When principal component analysis (PCA) was conducted, WT and N153S NP samples did not cleanly segregate (**Figure 6A**); however, hierarchical clustering of differentially expressed genes (DEGs)

defined by p ≤ 0.05 and an absolute fold change of two resulted in distinct clustering of WT and N153S NP profiles (**Figure 6B**). This profile included 327 DEGs, of which 134 were upregulated and 193 were downregulated, as shown by volcano plot (**Figure 6C**). To assess the biological significance of these genes, a statistical overrepresentation test (FDR < 0.05) was conducted in PANTHER, revealing no enrichment for any processes or pathways among DEGs. Among the most up- and downregulated DEGs in the NP were Phkb, Fam13a, and Ric1 and Olfr153, Pard3, and Kpna2, respectively (**Figure 6D**). By contrast, AF tissue profiles distinctly clustered by PCA (**Figure 6E**) and hierarchical clustering of DEGs (**Figure 6F**). Between WT and N153S AF tissues, 1321 DEGs – 856 upregulated and 465 downregulated – were identified (**Figure 6G**). As would be expected with STING activation, statistical overrepresentation tests for biological processes in PANTHER revealed immune system processes and their regulation to be those most enriched among upregulated DEGs (**Figure 6H**). Some of the select upregulated DEGs included *Retnlg*, *Sll*, *Lcp1*, and *Ctsg* (**Figure 6I**). Downregulated DEGs correlated to the broad ontologies of cellular and metabolic processes (**Figure 6J**). When DEGs from these processes were analyzed, the most downregulated genes within the categories were in alignment, including genes such as *Esrp2*, *Mup1*, *ND6*, *Adam23*, and *Serinc4* (**Figure 6K**). Taken together, these results indicate that at the
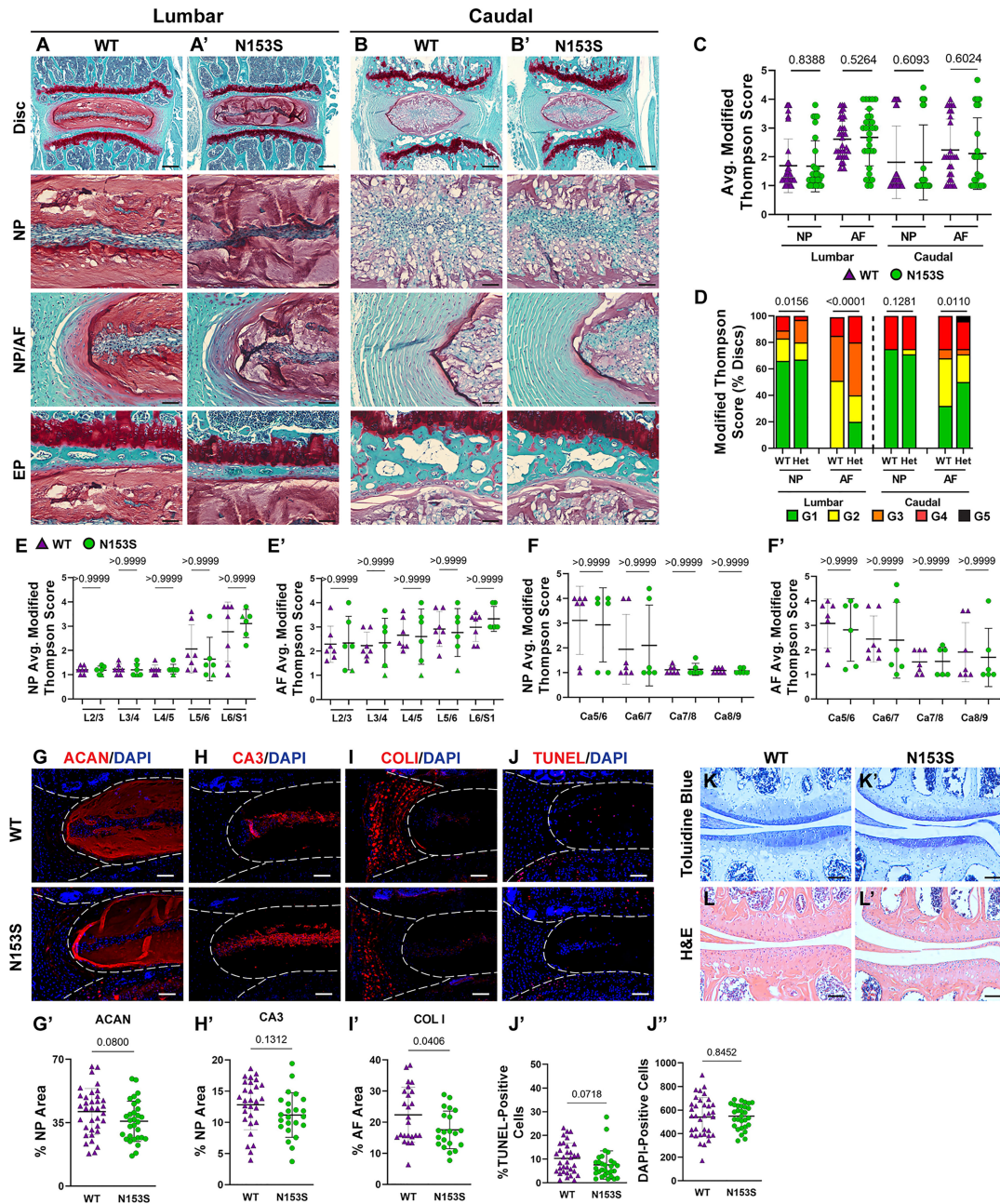
FIGURE 4 | Intervertebral discs and articular cartilage of N153S mice do not evidence accelerated degeneration. **(A-B')** 6-month-old WT and N153S mice were analyzed and Safranin O/Fast Green staining of **(A, A')** lumbar and **(B, B')** caudal discs shows tissue morphology and proteoglycan content (row 1, scale bar= 200 μm) and high magnification images of the NP, EP, and NP/AF tissue boundary (rows 2-4, scale bar= 50 μm) are shown. N153S discs retain vacuolated cells in the NP, demarcation between tissue compartments, and tissue architecture. **(C-F')** Histological grading assessment using the modified Thompson scale for **(E, E')** lumbar and **(F, F')** caudal discs (n = 5 lumbar discs/animal, 4 caudal discs/animal, 7 animals/genotype, 35 lumbar and 28 caudal discs/genotype). **(C)** average and **(D)** distribution of histological grades in the NP and AF, with higher scores indicating higher levels of degeneration. **(E, F')** Level-by-level average grades of NP and AF degeneration. **(G-I')** Quantitative immunohistological staining conducted on lumbar discs for: **(G)** aggrecan (ACAN), **(H)** carbonic anhydrase 3 (CA3), and **(I)** collagen I (COL I). **(G'-I')** Staining quantification demonstrating no change in ACAN and CA3 abundance and a slight reduction in COL I. **(J-J")** TUNEL staining showing apoptotic cells in the NP and AF regions of lumbar intervertebral disc sections from WT and N153S mice. **(H, I)** Corresponding quantification showing the percentage of TUNEL-positive cells and the number of DAPI-stained nuclei in the entire disc compartment. **(K, K')** Toluidine blue staining in the medial femoral condyle and tibial plateau shows no alteration to proteoglycan content and cartilage damage/loss. **(L, L')** H&E hindlimb staining showing no apparent cell death or osteophyte formation. (G-L' scale bar=100 μm) (n = 4 discs/animal, 7 animals/genotype, 28 total discs/genotype) (n = 1 joint/animal, 3 animals/genotype, 3 joints/genotype) Significance for grading distribution was determined using a χ^2 test. Significance of average and level-by-level grading and immunohistochemistry was determined using an unpaired t-test or Mann-Whitney test, as appropriate. Quantitative measurements represent mean ± SD.
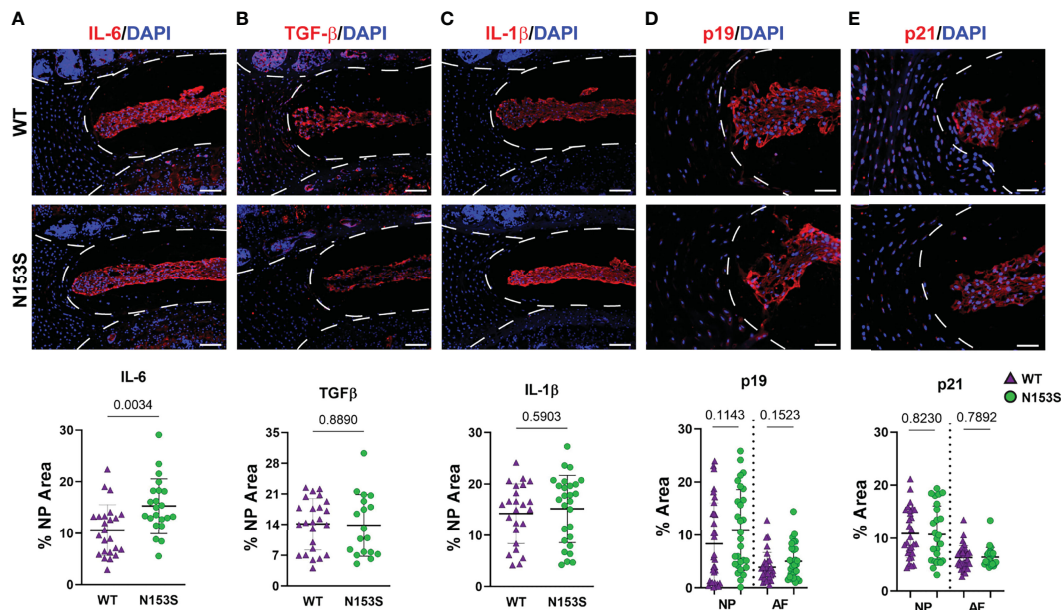
FIGURE 5 | SASP induction is not accelerated in the discs of N153S mice. Quantitative immunohistological staining conducted on 6-month-old WT and N153S lumbar discs for **(A, A')** IL-6, **(B, B')** TGF-β, **(C, C')** IL-1β, **(D, D')** p19, and **(E, E')** p21. Images were taken at 10x (scale bar = 100 μm). (n = 4 discs/animal; 7 animals/genotype, 28 total discs/genotype) Dotted lines demarcate different tissue compartments within the disc. Quantitative data represents the mean ± SD. Significance was determined using unpaired t-test or Mann-Whitney test, as appropriate.

transcriptomic level, STING activation more substantially impacts the AF than the NP, with upregulated genes enriching for immune and inflammatory processes.
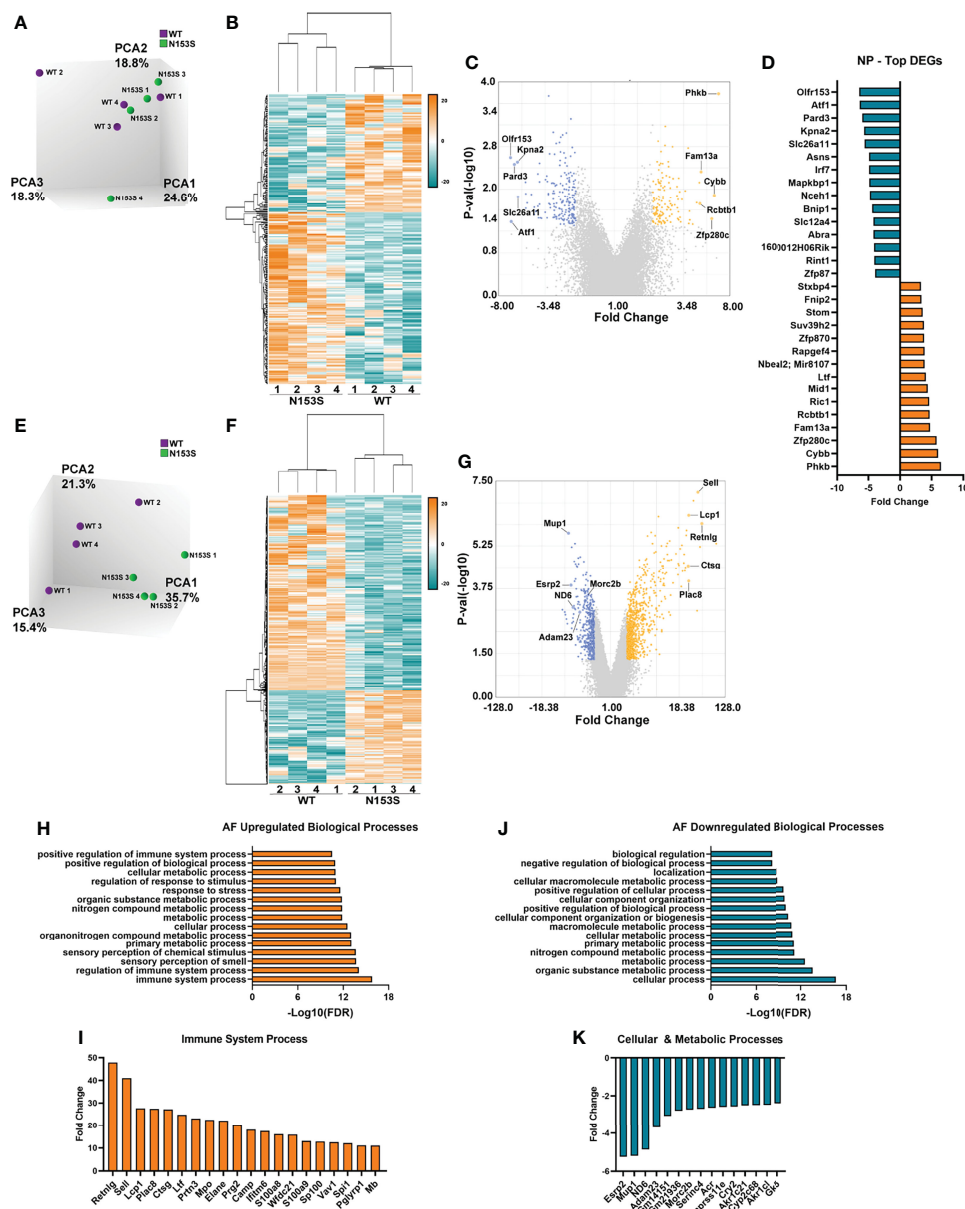
Transcriptomic Changes in the AF of N153S Mice Do Not Recapitulate Signatures of Human Degeneration

To investigate if the gene enrichment signatures observed in the AF tissues of N153S mice captured transcriptomic signatures of human AF degeneration, we analyzed human AF microarray data deposited by Kazezian *et al.* (GSE70362) (45). Principal component analysis (PCA) demonstrated that human AF samples did not cluster according to Thompson Grade (**Figure 7A**). For this reason, we conducted hierarchical clustering of the samples, with a cutoff of Euclidean distance < 0.5 (**Figure 7B**) (49). This resulted in four distinct clusters (green boxes) among healthy samples (grades 1 and 2) (n = 7), one mixed cluster (yellow box) consisting of healthy and degenerated samples (grades 1 and 3) (n = 2), and four clusters (pink boxes) among degenerated samples (grades 3, 4, and 5) (n = 15) (**Figure 7B**). For subsequent analyses, the healthy clusters were considered as a single group (H), and the mixed cluster (M) and degenerated clusters (D1, D2, D3, D4) were considered as individual clusters (**Figure 7C**); this clustering organized accordingly by principal components in three-dimensional space (though this is not captured by the two-dimensional rendering). Clusters D1-D4 and M were compared to cluster H, and the resultant up- and downregulated DEGs (p < 0.05, absolute fold change > 2) from each comparison were analyzed for enrichment of biological processes in PANTHER. Enriched processes were then analyzed against

processes enriched in N153S AF tissues. This analysis identified degenerated cluster 2 (D2) as sharing some overlap with the N153S results. Generalized biological and cellular processes were most overrepresented within D2 (**Figure 7D**), but processes did include immune and inflammatory response processes which aligned with those identified in the upregulated N153S data (**Figure 7E**). However, within these processes, only a few genes were commonly upregulated in human cluster D2 and N153S tissues, including BIRC3, CFD, RSAD2, and ALCAM – none of which are considered inflammatory hallmarks of disc degeneration (**Figure 7F**). When downregulated processes were assessed, multiple degenerated clusters showed some overlap with N153S results. This overlap was primarily restricted to generalized cellular, biological, and metabolic processes (**Figure 7G**), and there was no overlap in the genes influencing these processes, indicating that in terms of a downregulated transcriptional program, N153S AF tissues do not recapitulate broader immune related processes or signatures of degenerated human AF tissues.

Aged STING^{-/-} Mice Show Mild Structural Changes in the Vertebral Bone

To investigate the role of the cGAS-STING pathway in an aging context, we analyzed the spinal columns of 16-18-month-old STING^{-/-} mice. Lumbar (**Figures 8A, A'**) and caudal (**Figures 8B, B'**) vertebrae were assessed using μCT analyses. Caudal vertebrae in STING^{-/-} mice were longer than controls (**Figure 8C**), but the length of lumbar vertebrae was comparable between genotypes. In both spinal regions, disc height (**Figure 8D**) was unaltered by STING deletion, and the

FIGURE 6 | STING activation results in more prominent transcriptomic changes in the AF than the NP of N153S mice. **(A)** Principal component analysis (PCA) of 6-month-old WT and N153S NP tissues (n = 4 animals/genotype). **(B)** Heatmap of z-scores for NP DEGs defined by p < 0.05 and 2 < fold change < -2. **(C)** Volcano plot of DEG p-value plotted against fold change, showing 134 upregulated and 193 downregulated genes in N153S NP tissues. **(D)** DEGs identified in the NP with the greatest fold change. **(E)** PCA of 6-month-old WT and N153S AF tissues (n = 4 animals/genotype). **(F)** Heatmap of z-scores for AF DEGs defined by p < 0.05 and 2 < fold change < -2. **(G)** Volcano plot of DEG p-value plotted against fold change, showing 856 upregulated and 465 downregulated genes in N153S NP tissues. **(H)** Representative GO biological processes derived from upregulated genes in N153S AF tissues. **(I)** DEGs with the greatest fold change within the immune system process GO term. **(J)** Representative GO biological processes derived from downregulated genes in N153S AF tissues. **(K)** DEGs with the greatest fold change within the cellular process and metabolic process GO terms.

deviations in the caudal vertebral length did not translate to changes in the DHI (**Figure 8E**). Three-dimensional analyses of the trabecular bone revealed no changes in the lumbar spine and an increase in the trabecular number (**Figure 8F**) in the caudal vertebrae of STING$^{-/-}$ mice. Other trabecular properties of BV/TV (**Figure 8G**), trabecular thickness (**Figure 8H**), and

trabecular separation (**Figure 8I**) were consistent between genotypes. Analyses of the cortical shell demonstrated reduced bone volume (**Figure 8J**), cross-sectional thickness (**Figure 8K**), and bone area (**Figure 8L**) in the caudal vertebrae of STING$^{-/-}$ mice and no changes in the lumbar vertebrae. As seen in the N153S model, the consequences of STING deletion in the

FIGURE 7 | Transcriptomic changes in the AF of N153S mice do not recapitulate signatures of human degeneration. **(A)** Schematic showing PCA clustering based on Thompson Grades of human AF microarray samples (n = 24) deposited in GSE70362. **(B)** Hierarchical clustering of DEGs, p < 0.05 showed four healthy clusters (green boxes), one ambiguous cluster (yellow box), and four degenerated clusters (pink boxes), with a Euclidean distance cutoff of 0.5. **(C)** PCA of clusters obtained in B, where all healthy clusters were grouped into a single cluster, H. **(D)** Representative GO biological processes of upregulated genes between cluster D2 (degenerated) and cluster H (healthy). **(E)** GO biological processes of upregulated genes between D2 and H that overlap with N153S GO terms related to immune and inflammatory responses. **(F)** Fold change of upregulated DEGs related to an immune response that are common to D2 (dark green) and N153S (light green) transcriptomic profiles. **(G)** Schematic showing that downregulated genes in the AF of degenerated human AF tissues and N153S AF tissues broadly correlate to cellular, biological, and metabolic processes but diverge in terms of genes contributing to these broad categories of dysregulation.
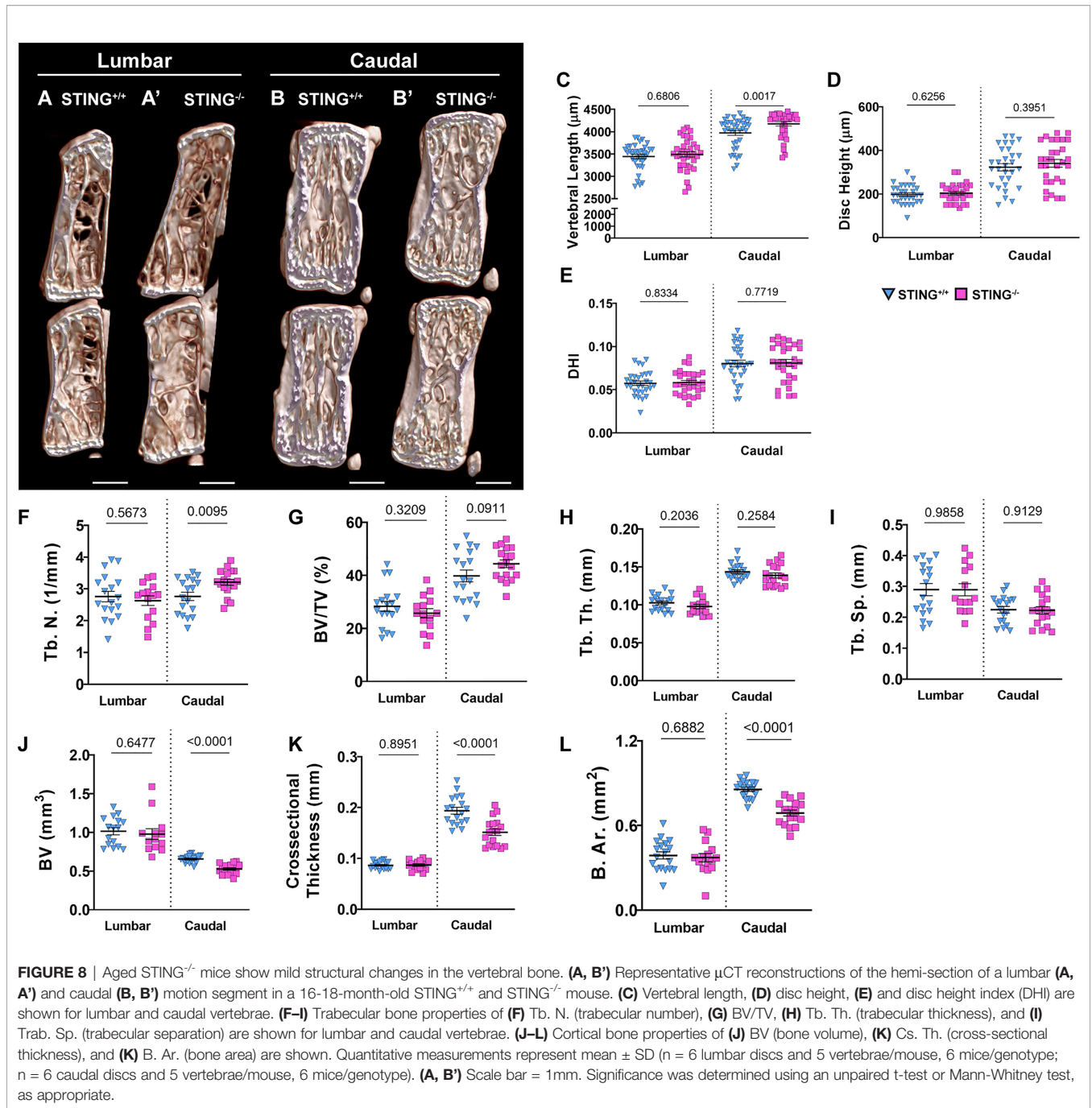
vertebrae are region-specific, with the caudal vertebrae demonstrating significant alterations in the cortical shell and trabeculae.

Aging STING$^{-/-}$ Mice Do Not Evidence Better Morphological Attributes and SASP Status in Disc

We assessed the impact of STING inactivation in delaying the onset of age-related degenerative changes in the disc. Safranin O/fast green and hematoxylin staining on average did not demonstrate better-preserved tissue architecture in the lumbar (**Figures 9A, A'**) or caudal (**Figures 9B, B'**) discs of 16-18-month-old STING$^{-/-}$ mice relative to STING$^{+/+}$ mice. Quantitative evaluation using the Modified Thompson grading scheme demonstrated slight differences in the distribution (**Figure 9C**) of lumbar NP scores, where no STING$^{-/-}$ discs scored a 3 or 4, and in caudal AF scores, for which distribution deviations did not

consistently demonstrate improved or worsened disc health, as STING$^{-/-}$ discs had higher proportions of grades 1 and 4. Despite these differences in score distributions, cumulative average grades (**Figure 9D**) did not vary across genotypes for either spinal region, and level-by-level analyses (**Figures 9E-F'**) did not indicate level-specific deviations, with the exception of the NP at L6/S1, where STING$^{-/-}$ discs averaged lower scores than controls. At the molecular level, immunohistochemical staining showed carbonic anhydrase 3 (**Figures 9G, G'**), aggrecan (**Figures 9H, H'**), and collagen IX (**Figures 9I, I'**) to be similarly abundant in the NP tissues of STING$^{-/-}$ and STING$^{+/+}$ mice. Abundance of key structural proteins collagen I (**Figures 9J, J'**) and cartilage oligomeric matrix protein (COMP) (**Figures 9K, K'**) was unchanged in the AF of STING$^{-/-}$ discs; however, these discs showed increased abundance of collagen II (**Figures 9L, L'**).

To further assess the overall collagen architecture and content of these discs, Picrosirius Red-stained discs from the

FIGURE 8 | Aged STING^{-/-} mice show mild structural changes in the vertebral bone. **(A, B')** Representative µCT reconstructions of the hemi-section of a lumbar **(A, A')** and caudal **(B, B')** motion segment in a 16-18-month-old STING^{+/+} and STING^{-/-} mouse. **(C)** Vertebral length, **(D)** disc height, **(E)** and disc height index (DHI) are shown for lumbar and caudal vertebrae. **(F–I)** Trabecular bone properties of **(F)** Tb. N. (trabecular number), **(G)** BV/TV, **(H)** Tb. Th. (trabecular thickness), and **(I)** Trab. Sp. (trabecular separation) are shown for lumbar and caudal vertebrae. **(J–L)** Cortical bone properties of **(J)** BV (bone volume), **(K)** Cs. Th. (cross-sectional thickness), and **(K)** B. Ar. (bone area) are shown. Quantitative measurements represent mean ± SD (n = 6 lumbar discs and 5 vertebrae/mouse, 6 mice/genotype; n = 6 caudal discs and 5 vertebrae/mouse, 6 mice/genotype). **(A, B')** Scale bar = 1mm. Significance was determined using an unpaired t-test or Mann-Whitney test, as appropriate.

lumbar (**Supplementary Figures 2A, A'**) and caudal (**Supplementary Figures 2B, B'**) spine were visualized under polarized light. Across both genotypes, the AF contained highly organized collagen fibrils, and no staining was detected in the NP. Quantitative analysis showed no differences in collagen fiber thickness distribution (**Supplementary Figure 2C**), indicating comparable rates of collagen turnover in knockout and wildtype discs. Fourier transform infrared (FTIR) spectroscopic imaging was used to assess the chemical composition of STING^{-/-} and STING^{+/+} discs. Spectral

clustering that groups and classifies individual pixels based on their chemical compositions showed no differences in the chemical composition of knockout and wildtype motion segments (**Supplementary Figures 2D, D'**). Average second derivative spectra were generated and analyzed for each disc compartment an the vertebrae at representative peaks for chondroitin sulfate (1064 cm^{-1}), cell-associated proteoglycans (1156 cm^{-1}), collagen (1338 cm^{-1}), and total protein (1660 cm^{-1}) (**Supplementary Figures 2E, E'**). Corresponding chemical maps (**Supplementary Figures 2F–I'**), quantified for each
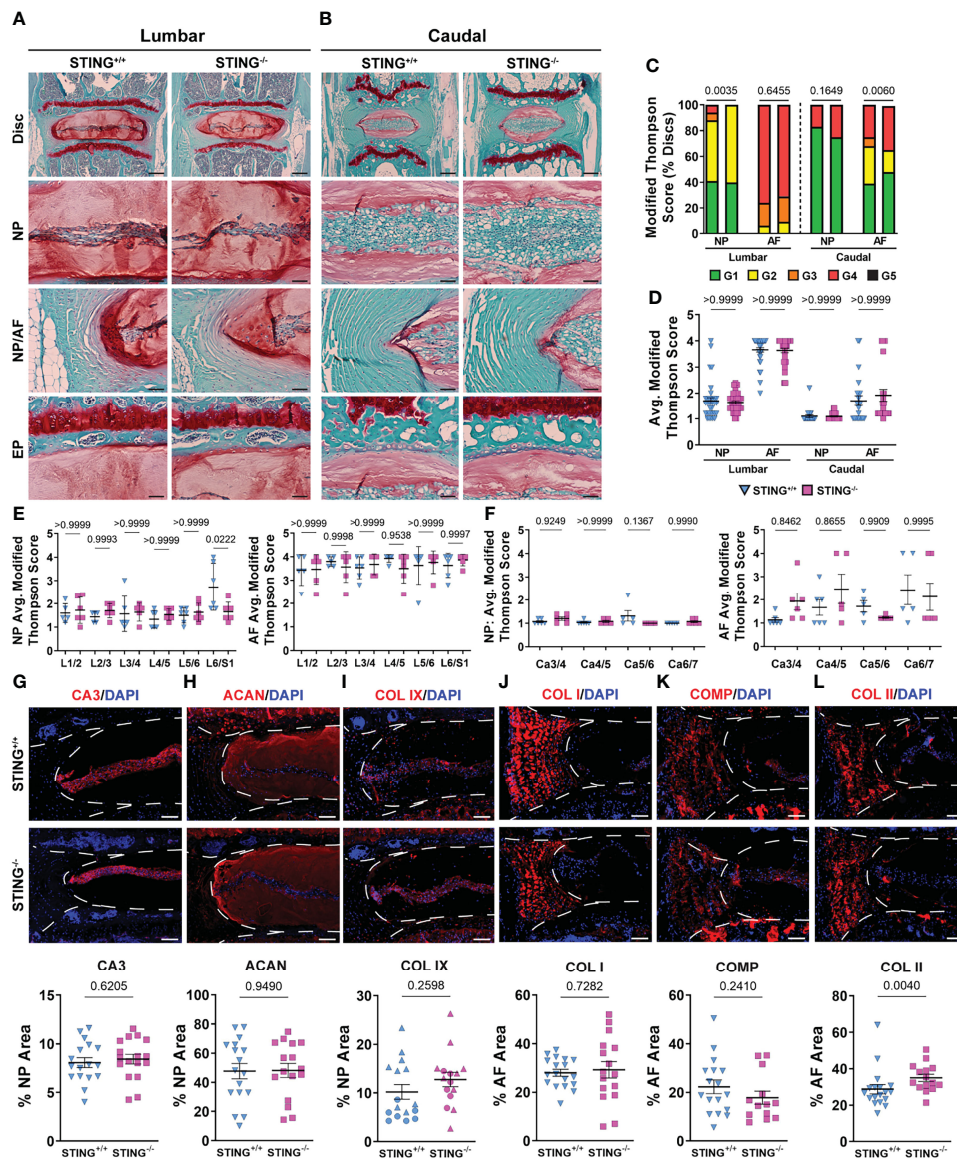
FIGURE 9 | STING$^{-/-}$ discs do not evidence an improved morphological or molecular phenotype. (A-B') 16-18-month-old STING$^{+/+}$ and STING$^{-/-}$ mice were analyzed and Safranin O/Fast Green staining of **(A, A')** lumbar and **(B, B')** caudal discs shows tissue morphology and proteoglycan content (row 1, scale bar= 200 μm) and high magnification images of the NP, EP, and NP/AF tissue boundary (rows 2-4, scale bar= 50 μm) are shown. **(C–F')** Histological grading assessment using the modified Thompson scale for **(E, E')** lumbar and **(F, F')** caudal discs (n = 5 lumbar discs/animal, 4 caudal discs/animal, 6 animals/genotype, 30 lumbar and 24 caudal discs/genotype). **(C)** Distribution of and **(D)** average histological grades in the NP and AF, with higher scores indicating higher levels of degeneration. **(E, F')** Level-by-level average grades of NP and AF degeneration. **(G–L')** Quantitative immunohistological staining conducted on lumbar discs for **(A, A')** CA3, **(B, B')** ACAN, **(C, C')** collagen IX (COL IX), **(J, J')** COL I, **(K, K')** collagen oligomeric matrix protein (COMP), and **(L, L')** collagen II (COL II). (n = 2-4 discs/animal; 6 animals/genotype, 12-24 total discs/genotype) Dotted lines demarcate different tissue compartments within the disc. Significance for grading distribution was determined using a χ^2 test. Significance of average and level-by-level scores and quantified immunohistochemistry was determined using an unpaired t-test or Mann-Whitney test, as appropriate. Quantitative measurements represent mean ± SD.

molecular class in each tissue (**Supplementary Figures 2F''-G''**), revealed only a slight reduction in the collagen content of the NP, without any significant changes to chondroitin sulfate, cell-associated proteoglycans, or total protein content. Taken in context with the histological evaluation of STING$^{-/-}$ and STING$^{+/+}$ mice, this chemical analysis indicates STING

inactivation does not confer an advantage to any of the disc compartments during aging.

Again considering the possibility that a molecular phenotype may manifest in the absence in a morphological phenotype, we conducted immunohistological staining for known SASP markers to determine if the loss of STING attenuated delayed the onset of

senescence. Interestingly, IL-1β was more abundant in knockout discs than in wildtype discs (**Supplementary Figures 3A, A'**), but IL-6 (**Supplementary Figures 3B, B'**), TGF-β (**Supplementary Figures 3C, C'**), p19 (**Supplementary Figures 3D, D'**), and p21 (**Supplementary Figures 3E, E'**) were unchanged, indicating loss of STING does not delay cell senescence or SASP onset. Taken together, our analyses of N153S and STING$^{-/-}$ mice for the first time demonstrate that the cGAS-STING pathway is not a critical regulator of senescence and consequent degeneration of the intervertebral disc *in vivo*.

DISCUSSION

Cellular senescence is well-established as a feature of aging and degeneration in the human intervertebral disc as well as various mouse models (13, 17, 19, 52). Of interest, cellular senescence is shown to destabilize the nuclear membrane, resulting in the release of cytosolic chromatin fragments and consequent activation of the cGAS-STING pathway (24). This DNA-sensing pathway promotes SASP and mediates type-I interferon inflammatory responses to foreign viral and bacterial DNA as well as self-DNA (22). Cursory studies of NP cells and *in vivo* injury models have implicated the cGAS-STING pathway as an active inducer of senescence in the disc; however, this pathway in the disc is yet to be explored independent of chemical or mechanical insult (27, 28, 53–55). In this study, we clearly show STING is not a critical mediator of senescence onset and consequent degeneration in the disc. Detailed analyses of the spinal columns of 6-month-old heterozygous N153S mice with a gain-of-function mutation in the *Sting1* gene and 16-18-month-old STING$^{-/-}$ mice revealed healthy disc tissues in both genotypes with some compromised features of the vertebrae.

The gain-of-function STING mutation resulted in a significant increase in the plasma concentration of pro-inflammatory molecules IL-1β, IL-6, TNF-α, IFN-γ, MIP-1α/CCL3, IL-2, IL-27/p28/IL-30, MCP-1, and IP-10 in N153S mice. N153S animals have also been shown to overexpress IL-1β, IL-6, and MIP-1α in their lungs as an attribute of the vasculopathy they experience (31). The increased systemic cytokine concentrations are indicative of the hypercytokinemia that occurs as a consequence of cGAS-STING activity; as an immune and antitumor response, this cytokine "storm" is capable of causing cell toxicity and death, which is advantageous as a defense mechanism but otherwise detrimental (22, 56). These results underscored an environment of systemic inflammation, which could have broader consequences for the health of spinal column. One such consequence may be the reduction in bone volume observed in the trabecular and cortical bone of the caudal vertebrae in N153S mice. All of the pro-inflammatory markers upregulated in the plasma are associated with macrophages as either proinflammatory secretions or macrophage activators (57). Staining of F4/80, MHC II, and Ly-6G in the vertebrae showed greater macrophage and monocyte abundance and activation in N153S vertebrae as an effect of STING activation. Importantly, a higher abundance of MHC II in this inflammatory milieu suggested these were activated

macrophages, which would support the changes observed by μCT in the vertebrae as being osteoclast driven. Despite higher macrophage and monocyte abundance, TRAP staining did not evidence more osteoclasts in N153S vertebrae. However, it is important to recognize that bone resorption is a highly dynamic process, and the trabecular and cortical changes in the N153S vertebrae are relatively minor, so it is possible that this incongruence in activated osteoclasts and macrophage abundance is the result of examining a static window during which the osteoclast population is less active. Previous studies have correlated STING expression with elevated osteoblastic activity in a model of DNA damage-induced inflammation (DNaseII$^{-/-}$, IFNR$^{-/-}$), but IL-1β, IL-6, TNF-α stimulate osteoclast differentiation, which may also explain the compromised bone quality in N153S mice (26, 58, 59). Of note, recent work demonstrated STING induction through DMXAA treatment in mice attenuates cancer-induced osteoclast differentiation in the femur through type I interferon signaling and that STING induction inhibited bone fracture-induced pain by suppressing nociceptor excitability (60). These results show an opposite effect of STING activation on bone cells in the femur than that observed in the vertebrae in the present study; one possible explanation for such is the impact of proinflammatory signaling in the absence of direct insult to the tissue as opposed to in the context of injury or a diseased tissue microenvironment.

Further, despite the proinflammatory circulating cytokine profile and mild vertebral phenotype, histological analyses demonstrated that STING activation did not accelerate a degenerative phenotype in the NP, AF, EP, or articular cartilage. This was somewhat surprising considering arthritis is a symptom of SAVI, the disease recapitulated by the N153S mutation (61). The findings in the disc do however align with the recent work of Gorth *et al.* in hTNF-α overexpression mouse models and contribute to a growing body of evidence demonstrating the marginal impacts of systemic inflammation on overall disc health (30, 62). Other *in vivo* models of systemic inflammation, including high fat diet-induced obesity, have shown disc and articular cartilage architecture are not negatively impacted by systemic inflammatory conditions (63, 64). This can likely be attributed to the lack of vasculature in both tissues. The avascular and hypoxic nature of the intervertebral disc confers immune privilege to the tissue, protecting it from circulating inflammatory cytokines that are detrimental to well-vascularized skeletal tissues like bone (65). Articular cartilage similarly demonstrates immune privileged properties and immunomodulatory effects, which contribute to the ability of the uninjured tissue to resist negative consequences in a proinflammatory environment (66, 67). Animals in this study were analyzed at 6 months, and as seen in the structurally intact discs of these models, N153S NP tissues retained healthy, vacuolated cells expressing the NP-phenotypic marker CA3 and an aggrecan-rich matrix. Unlike the hTNF-α models, the AF was structurally uncompromised by constitutive STING activation, demonstrating a reduction in collagen 1 abundance without impact on the organization or structure of the tissue. This reduction in collagen 1 may be indicative of an early

remodeling response of the outer AF, which interacts most directly with the systemic environment (68). AF tissues of N153S mice also upregulated over 100 genes related to an immune response, including *il1b, il1rn, ifitm6, cdk1, ifitm3*, and *tnfaip2*. This gene signature, however, did not tightly correlate to structural attributes of the AF nor correlate with a gene signature associated with disc degeneration in human AF tissues. Marginal overlap between the results of N153S and degenerated human AF tissues indicates the possibility for STING activation to eventually facilitate the degenerative process, but at the time of analysis, STING activation did not promote a transcriptional program associated with human disc degeneration. Considering the NP tissues of N153S animals, despite an increase in IL-6, which is known to be strongly induced by STING in other systems, the overall onset of senescence and induction of SASP were not accelerated by STING gain-of-function, evidenced by unaltered TGF-β, p19, and p21 levels (69). Consistent with reports showing IL-6 knockout mice are prone to osteoarthritis also suggesting a homeostatic function of this cytokine, the increase in IL-6 in the NP of N153S mice may imply a stress or compensatory response to maintain disc homeostasis (70, 71). Overall, this analysis supports that the NP is largely isolated from the consequences of systemic inflammation and that systemic inflammation does not necessarily promote disc degeneration. Since N153S animals were analyzed at 6 months, it is conceivable that as the mice age, STING activation could promote senescence and degeneration. However, despite strong pathological changes in the blood vessels, lungs, spleen, and bone of these mice, the disc shows only mild changes, making it unlikely that further aging will result in a strong degenerative phenotype driven by STING activation (29, 31, 47).

With the role of cellular senescence in aging in mind, it remained possible that in aged mice – when senescence is known to occur in the disc – the deletion of STING would be protective to the spinal column by delaying the onset of senescence. μCT analyses of 16-18-month-old STING$^{-/-}$ vertebrae showed that the loss of STING in the caudal vertebrae resulted in longer bones with fewer trabeculae and an overall reduction in the structural properties of the cortical shell. This finding is interesting in that cortical thinning and reduced bone mass have been associated with systemic inflammation clinically and in mouse models, but STING$^{-/-}$ tissues have been shown to express lower levels of inflammatory markers than STING$^{+/+}$ tissues (24, 30, 72). One possible explanation for this contradiction is the apparent impact of STING on the balance between osteoblast and osteoclast activity, as suggested by Baum et al. (26).

Similarly to the N153S model, histological and spectroscopic analyses of the discs revealed STING loss did not significantly improve aging outcomes. Aged STING$^{-/-}$ and STING$^{+/+}$ discs maintained healthy disc architecture and cellularity, as reflected by low Modified Thompson scores and comparable levels of key structural proteins, including aggrecan, collagen IX, collagen I, and COMP. STING$^{-/-}$ discs did evidence higher abundance of collagen II; however, collagen fiber thickness distribution and chemical mapping demonstrated overall consistency across genotypes. This

was also true for SASP markers IL-6, TGF-β, p19, and p21, with STING$^{-/-}$ discs showing increased levels of IL-1β. By contrast, in mice where senescent cells have been targeted with deletion of p16INK4A, disc architecture was similarly unimpacted, but SASP was reduced (19). In the present study, STING$^{+/+}$ NP structure was well-preserved with age, and the AF exhibited some degeneration. STING deletion did not however reduce the severity of degeneration in the AF, and senescence and SASP marker burden were unchanged, contrasting directly to the aforementioned model using p16 removal. These results strongly support that STING is not a major effector of senescence in the natural aging and degeneration context. Recent work has demonstrated cGAS-STING activation in a LPS vertebral injury-induced disc degeneration model; however, this activation was only achieved with the inflammatory stimulus of LPS and by breaching the integrity of the EP, enabling immune cell infiltration into the disc compartment (27). Similarly, a recent study showed the degenerative effects of needle puncture injury to rat discs were reduced when STING activation was attenuated by limiting mitochondrial DNA release from damaged mitochondria resulting from calcium overload (28). It is likely, however, that in the context of this acute herniation injury, infiltrating scavenging immune cells such as neutrophils and macrophages were the primary effectors of the cGAS-STING response and responsible for promoting inflammation; a similar immune response has been documented in the Tg197 mouse model, which overexpresses hTNFα and is predisposed to spontaneous disc herniations (62). Our work clearly demonstrates that in the absence of chemical or traumatic mechanical insult, STING activity at the timepoints analyzed neither accelerates nor attenuates the onset of cellular senescence and the degeneration cascade in the intervertebral disc. Accordingly, while the cGAS-STING pathway is a critical modulator of cellular senescence in other systems, it is unlikely to be an effective target for mitigating degeneration and cell senescence in the disc.

DATA AVAILABILITY STATEMENT

ETHICS STATEMENT

AUTHOR CONTRIBUTIONS

SUPPLEMENTARY MATERIAL

The Supplementary Material for this article can be found online at: https://www.frontiersin.org/articles/10.3389/fimmu.2022.882407/full#supplementary-material

REFERENCES

1. Livshits G, Popham M, Malkin I, Sambrook PN, Macgregor AJ, Spector T, et al. Lumbar Disc Degeneration and Genetic Factors Are the Main Risk Factors for Low Back Pain in Women: The UK Twin Spine Study. *Ann Rheum Dis* (2011) 70(10):1740–5. doi: 10.1136/ard.2010.137836
2. GBD 2017 Disease and Injury Incidence and Prevalence Collaborators. Global, Regional, and National Incidence, Prevalence, and Years Lived With Disability for 354 Diseases and Injuries for 195 Countries and Territories, 1990-2017: A Systematic Analysis for the Global Burden of Disease Study 2017. *Lancet* (2018) 392(10159):1789–858. doi: 10.1016/S0140-6736(18)32279-7
3. Silagi ES, Schipani E, Shapiro IM, Risbud MV. The Role of HIF Proteins in Maintaining the Metabolic Health of the Intervertebral Disc. *Nat Rev Rheumatol* (2021) 17(7):426–39. doi: 10.1038/s41584-021-00621-2
4. Silagi ES, Schoepflin ZR, Seifert EL, Merceron C, Schipani E, Shapiro IM, et al. Bicarbonate Recycling by HIF-1-Dependent Carbonic Anhydrase Isoforms 9 and 12 Is Critical in Maintaining Intracellular pH and Viability of Nucleus Pulposus Cells. *J Bone Miner Res* (2018) 33(2):338–55. doi: 10.1002/jbmr.3293
5. Novais EJ, Choi H, Madhu V, Suyama K, Anjo SI, Manadas B, et al. Hypoxia and Hypoxia-Inducible Factor-1α Regulate Endoplasmic Reticulum Stress in Nucleus Pulposus Cells: Implications of Endoplasmic Reticulum Stress for Extracellular Matrix Secretion. *Am J Pathol* (2021) 191(3):487–502. doi: 10.1016/j.ajpath.2020.11.012
6. Madhu V, Boneski PK, Silagi E, Qiu Y, Kurland I, Guntur AR, et al. Hypoxic Regulation of Mitochondrial Metabolism and Mitophagy in Nucleus Pulposus Cells Is Dependent on HIF-1α-BNIP3 Axis. *J Bone Miner Res* (2020) 35(8):1504–24. doi: 10.1002/jbmr.4019
7. Rajpurohit R, Risbud MV, Ducheyne P, Vresilovic EJ, Shapiro IM. Phenotypic Characteristics of the Nucleus Pulposus: Expression of Hypoxia Inducing Factor-1, Glucose Transporter-1 and MMP-2. *Cell Tissue Res* (2002) 308(3):401–7. doi: 10.1007/s00441-002-0563-6
8. Dolor A, Sampson SL, Lazar AA, Lotz JC, Szoka FC, Fields AJ. Matrix Modification for Enhancing the Transport Properties of the Human Cartilage Endplate to Improve Disc Nutrition. *PloS One* (2019) 14(4):e0215218. doi: 10.1371/journal.pone.0215218
9. Sivan SS, Wachtel E, Roughley P. Structure, Function, Aging and Turnover of Aggrecan in the Intervertebral Disc. *Biochim Biophys Acta* (2014) 1840(10):3181–9. doi: 10.1016/j.bbagen.2014.07.013
10. Choi H, Tessier S, Silagi ES, Kyada R, Yousefi F, Pleshko N, et al. A Novel Mouse Model of Intervertebral Disc Degeneration Shows Altered Cell Fate and Matrix Homeostasis. *Matrix Biol* (2018) 70:102–22. doi: 10.1016/j.matbio.2018.03.019
11. Cheung KMC, Karppinen J, Chan D, Ho DWH, Song Y-Q, Sham P, et al. Prevalence and Pattern of Lumbar Magnetic Resonance Imaging Changes in a Population Study of One Thousand Forty-Three Individuals. *Spine* (2009) 34(9):934–40. doi: 10.1097/BRS.0b013e3181a01b3f
12. Kim K-W, Chung H-N, Ha K-Y, Lee J-S, Kim Y-Y. Senescence Mechanisms of Nucleus Pulposus Chondrocytes in Human Intervertebral Discs. *Spine J* (2009) 9(8):658–66. doi: 10.1016/j.spinee.2009.04.018
13. Le Maitre CL, Freemont AJ, Hoyland JA. Accelerated Cellular Senescence in Degenerate Intervertebral Discs: A Possible Role in the Pathogenesis of

Intervertebral Disc Degeneration. *Arthritis Res Ther* (2007) 9(3):R45. doi: 10.1186/ar2198
14. Gruber HE, Ingram JA, Norton HJ, Hanley EN. Senescence in Cells of the Aging and Degenerating Intervertebral Disc: Immunolocalization of Senescence-Associated Beta-Galactosidase in Human and Sand Rat Discs. *Spine* (2007) 32(3):321–7. doi: 10.1097/01.brs.0000253960.57051.de
15. Sessions GA, Copp ME, Liu J-Y, Sinkler MA, D'Costa S, Diekman BO. Controlled Induction and Targeted Elimination of P16ink4a-Expressing Chondrocytes in Cartilage Explant Culture. *FASEB J* (2019) 33(11):12364–73. doi: 10.1096/fj.201900815RR
16. Nasto LA, Wang D, Robinson AR, Clauson CL, Ngo K, Dong Q, et al. Genotoxic Stress Accelerates Age-Associated Degenerative Changes in Intervertebral Discs. *Mech Ageing Dev* (2013) 134(1-2):35–42. doi: 10.1016/j.mad.2012.11.002
17. Ngo K, Patil P, McGowan SJ, Niedernhofer LJ, Robbins PD, Kang J, et al. Senescent Intervertebral Disc Cells Exhibit Perturbed Matrix Homeostasis Phenotype. *Mech Ageing Dev* (2017) 166:16–23. doi: 10.1016/j.mad.2017.08.007
18. Coppé J-P, Desprez P-Y, Krtolica A, Campisi J. The Senescence-Associated Secretory Phenotype: The Dark Side of Tumor Suppression. *Annu Rev Pathol* (2010) 5:99–118. doi: 10.1146/annurev-pathol-121808-102144
19. Novais EJ, Diekman BO, Shapiro IM, Risbud MV. p16Ink4a Deletion in Cells of the Intervertebral Disc Affects Their Matrix Homeostasis and Senescence Associated Secretory Phenotype Without Altering Onset of Senescence. *Matrix Biol* (2019) 82:54–70. doi: 10.1016/j.matbio.2019.02.004
20. Cherif H, Bisson DG, Mannarino M, Rabau O, Ouellet JA, Haglund L. Senotherapeutic Drugs for Human Intervertebral Disc Degeneration and Low Back Pain. *Elife* (2020, 9:9. doi: 10.7554/eLife.54693
21. Novais EJ, Tran VA, Johnston SN, Darris KR, Roupas AJ, Sessions GA, et al. Long-Term Treatment With Senolytic Drugs Dasatinib and Quercetin Ameliorates Age-Dependent Intervertebral Disc Degeneration in Mice. *Nat Commun* (2021) 12(1):5213. doi: 10.1038/s41467-021-25453-2
22. Li T, Chen ZJ. The cGAS-cGAMP-STING Pathway Connects DNA Damage to Inflammation, Senescence, and Cancer. *J Exp Med* (2018) 215(5):1287–99. doi: 10.1084/jem.20180139
23. Ivanov A, Pawlikowski J, Manoharan I, van Tuyn J, Nelson DM, Rai TS, et al. Lysosome-Mediated Processing of Chromatin in Senescence. *J Cell Biol* (2013) 202(1):129–43. doi: 10.1083/jcb.201212110
24. Dou Z, Ghosh K, Vizioli MG, Zhu J, Sen P, Wangensteen KJ, et al. Cytoplasmic Chromatin Triggers Inflammation in Senescence and Cancer. *Nat* (2017) 550(7676):402–6. doi: 10.1038/nature24050
25. Baum R, Sharma S, Carpenter S, Li Q-Z, Busto P, Fitzgerald KA, et al. Cutting Edge: AIM2 and Endosomal TLRs Differentially Regulate Arthritis and Autoantibody Production in DNase II-Deficient Mice. *J Immunol* (2015) 194(3):873–7. doi: 10.4049/jimmunol.1402573
26. Baum R, Sharma S, Organ JM, Jakobs C, Hornung V, Burr DB, et al. STING Contributes to Abnormal Bone Formation Induced by Deficiency of Dnase II in Mice. *Arthritis Rheumatol* (2017) 69(2):460–71. doi: 10.1002/art.39863
27. Su Q, Cai Q, Li Y, Ge H, Zhang Y, Zhang Y, et al. A Novel Rat Model of Vertebral Inflammation-Induced Intervertebral Disc Degeneration Mediated by Activating cGAS/STING Molecular Pathway. *J Cell Mol Med* (2021) 25:9567–85. doi: 10.1111/jcmm.16898

28. Zhang W, Li G, Luo R, Lei J, Song Y, Wang B, et al. Cytosolic Escape of Mitochondrial DNA Triggers cGAS-STING-NLRP3 Axis-Dependent Nucleus Pulposus Cell Pyroptosis. *Exp Mol Med* (2022) 54:129–42. doi: 10.1038/s12276-022-00729-9

29. Warner JD, Irizarry-Caro RA, Bennion BG, Ai TL, Smith AM, Miner CA, et al. STING-Associated Vasculopathy Develops Independently of IRF3 in Mice. *J Exp Med* (2017) 214(11):3279–92. doi: 10.1084/jem.20171351

30. Gorth DJ, Ottone OK, Shapiro IM, Risbud MV. Differential Effect of Long-Term Systemic Exposure of Tnfα on Health of the Annulus Fibrosus and Nucleus Pulposus of the Intervertebral Disc. *J Bone Miner Res* (2020) 35 (4):725–37. doi: 10.1002/jbmr.3931

31. Luksch H, Stinson WA, Platt DJ, Qian W, Kalugotla G, Miner CA, et al. STING-Associated Lung Disease in Mice Relies on T Cells But Not Type I Interferon. *J Allergy Clin Immunol* (2019) 144(1):254–266.e8. doi: 10.1016/j.jaci.2019.01.044

32. Ishikawa H, Barber GN. STING is an Endoplasmic Reticulum Adaptor That Facilitates Innate Immune Signalling. *Nat* (2008) 455(7213):674–8. doi: 10.1038/nature07317

33. Tajerian M, Alvarado S, Millecamps M, Dashwood T, Anderson KM, Haglund L, et al. DNA Methylation of SPARC and Chronic Low Back Pain. *Mol Pain* (2011) 7:65. doi: 10.1186/1744-8069-7-65

34. Silagi ES, Novais EJ, Bisetto S, Telonis AG, Snuggs J, Le Maitre CL, et al. Lactate Efflux From Intervertebral Disc Cells Is Required for Maintenance of Spine Health. *J Bone Miner Res* (2020) 35(3):550–70. doi: 10.1002/jbmr.3908

35. Park J, Fertala A, Tomlinson RE. Naproxen Impairs Load-Induced Bone Formation, Reduces Bone Toughness, and Diminishes Woven Bone Formation Following Stress Fracture in Mice. *Bone* (2019) 124:22–32. doi: 10.1016/j.bone.2019.04.009

36. Boneski PK, Madhu V, Tomlinson RE, Shapiro IM, van de Wetering K, Risbud MV. Abcc6 Null Mice—A Model for Mineralization Disorder PXE Shows Vertebral Osteopenia Without Enhanced Intervertebral Disc Calcification With Aging. *Front Cell Dev Biol* (2022) 10:10. doi: 10.3389/fcell.2022.823249

37. Thompson JP, Pearce RH, Schechter MT, Adams ME, Tsang IK, Bishop PB. Preliminary Evaluation of a Scheme for Grading the Gross Morphology of the Human Intervertebral Disc. *Spine* (1990) 15(5):411–5. doi: 10.1097/00007632-199005000-00012

38. Armstrong AR, Carlson CS, Rendahl AK, Loeser RF. Optimization of Histologic Grading Schemes in Spontaneous and Surgically-Induced Murine Models of Osteoarthritis. *Osteoarthr Cartil* (2021) 29(4):536–46. doi: 10.1016/j.joca.2021.01.006

39. McNulty MA, Loeser RF, Davey C, Callahan MF, Ferguson CM, Carlson CS. A Comprehensive Histological Assessment of Osteoarthritis Lesions in Mice. *Cartilage* (2011) 2(4):354–63. doi: 10.1177/1947603511402665

40. Dyment NA, Breidenbach AP, Schwartz AG, Russell RP, Aschbacher-Smith L, Liu H, et al. Gdf5 Progenitors Give Rise to Fibrocartilage Cells That Mineralize *via* Hedgehog Signaling to Form the Zonal Enthesis. *Dev Biol* (2015) 405 (1):96–107. doi: 10.1016/j.ydbio.2015.06.020

41. Schindelin J, Arganda-Carreras I, Frise E, Kaynig V, Longair M, Pietzsch T, et al. Fiji: An Open-Source Platform for Biological-Image Analysis. *Nat Methods* (2012) 9(7):676–82. doi: 10.1038/nmeth.2019

42. Kobrina Y, Rieppo L, Saarakkala S, Jurvelin JS, Isaksson H. Clustering of Infrared Spectra Reveals Histological Zones in Intact Articular Cartilage. *Osteoarthr Cartil* (2012) 20(5):460–8. doi: 10.1016/j.joca.2012.01.014

43. Thomas PD, Campbell MJ, Kejariwal A, Mi H, Karlak B, Daverman R, et al. PANTHER: A Library of Protein Families and Subfamilies Indexed by Function. *Genome Res* (2003) 13(9):2129–41. doi: 10.1101/gr.772403

44. Thomas PD, Kejariwal A, Guo N, Mi H, Campbell MJ, Muruganujan A, et al. Applications for Protein Sequence-Function Evolution Data: mRNA/Protein Expression Analysis and Coding SNP Scoring Tools. *Nucleic Acids Res* (2006) 34(Web Server issue):W645–50. doi: 10.1093/nar/gkl229

45. Kazezian Z, Gawri R, Haglund L, Ouellet J, Mwale F, Tarrant F, et al. Gene Expression Profiling Identifies Interferon Signalling Molecules and IGFBP3 in Human Degenerative Annulus Fibrosus. *Sci Rep* (2015) 5:15662. doi: 10.1038/srep15662

46. Martin GR, Henare K, Salazar C, Scheidl-Yee T, Eggen LJ, Tailor PP, et al. Expression of a Constitutively Active Human STING Mutant in Hematopoietic Cells Produces an Ifnar1-Dependent Vasculopathy in Mice. *Life Sci Alliance* (2019) 2(3):1–15. doi: 10.26508/lsa.201800215

47. Siedel H, Roers A, Rösen-Wolff A, Luksch H. Type I Interferon-Independent T Cell Impairment in a Tmem173 N153S/WT Mouse Model of STING Associated Vasculopathy With Onset in Infancy (SAVI). *Clin Immunol* (2020) 216:108466. doi: 10.1016/j.clim.2020.108466

48. Tsingas M, Ottone OK, Haseeb A, Barve RA, Shapiro IM, Lefebvre V, et al. Sox9 Deletion Causes Severe Intervertebral Disc Degeneration Characterized by Apoptosis, Matrix Remodeling, and Compartment-Specific Transcriptomic Changes. *Matrix Biol* (2020) 94:110–33. doi: 10.1016/j.matbio.2020.09.003

49. Novais EJ, Tran VA, Miao J, Slaver K, Sinensky A, Dyment NA, et al. Comparison of Inbred Mouse Strains Shows Diverse Phenotypic Outcomes of Intervertebral Disc Aging. *Aging Cell* (2020) 19(5):e13148. doi: 10.1111/acel.13148

50. Tessier S, Doolittle AC, Sao K, Rotty JD, Bear JE, Ulici V, et al. Arp2/3 Inactivation Causes Intervertebral Disc and Cartilage Degeneration With Dysregulated TonEBP-Mediated Osmoadaptation. *JCI Insight* (2020) 5 (4):1–19. doi: 10.1172/jci.insight.131382

51. Tessier S, Tran VA, Ottone OK, Novais EJ, Doolittle A, DiMuzio MJ, et al. TonEBP-Deficiency Accelerates Intervertebral Disc Degeneration Underscored by Matrix Remodeling, Cytoskeletal Rearrangements, and Changes in Proinflammatory Gene Expression. *Matrix Biol* (2020) 87:94–111. doi: 10.1016/j.matbio.2019.10.007

52. Roberts S, Evans EH, Kletsas D, Jaffray DC, Eisenstein SM. Senescence in Human Intervertebral Discs. *Eur Spine J* (2006) 15 Suppl 3:S312–6. doi: 10.1007/s00586-006-0126-8

53. Tian Y, Bao Z, Ji Y, Mei X, Yang H. Epigallocatechin-3-Gallate Protects H2O2-Induced Nucleus Pulposus Cell Apoptosis and Inflammation by Inhibiting cGAS/Sting/NLRP3 Activation. *Drug Des Devel Ther* (2020) 14:2113–22. doi: 10.2147/DDDT.S251623

54. Guo Q, Zhu D, Wang Y, Miao Z, Chen Z, Lin Z, et al. Targeting STING Attenuates ROS Induced Intervertebral Disc Degeneration. *Osteoarthr Cartil* (2021) 29:1213–24. doi: 10.1016/j.joca.2021.04.017

55. Chen Z, Yang X, Zhou Y, Liang Z, Chen C, Han C, et al. Dehydrocostus Lactone Attenuates the Senescence of Nucleus Pulposus Cells and Ameliorates Intervertebral Disc Degeneration *via* Inhibition of STING-TBK1/NF-κb and MAPK Signaling. *Front Pharmacol* (2021) 12:641098. doi: 10.3389/fphar.2021.641098

56. Zhang C, Liang Z, Ma S, Liu X. Radiotherapy and Cytokine Storm: Risk and Mechanism. *Front Oncol* (2021) 11:670464. doi: 10.3389/fonc.2021.670464

57. Arango Duque G, Descoteaux A. Macrophage Cytokines: Involvement in Immunity and Infectious Diseases. *Front Immunol* (2014) 5:491. doi: 10.3389/fimmu.2014.00491

58. Ragab AA, Nalepka JL, Bi Y, Greenfield EM. Cytokines Synergistically Induce Osteoclast Differentiation: Support by Immortalized or Normal Calvarial Cells. *Am J Physiol Cell Physiol* (2002) 283(3):C679–87. doi: 10.1152/ajpcell.00421.2001

59. Steeve KT, Marc P, Sandrine T, Dominique H, Yannick F. IL-6, RANKL, TNF-Alpha/IL-1: Interrelations in Bone Resorption Pathophysiology. *Cytokine Growth Factor Rev* (2004) 15(1):49–60. doi: 10.1016/j.cytogfr.2003.10.005

60. Wang K, Donnelly CR, Jiang C, Liao Y, Luo X, Tao X, et al. STING Suppresses Bone Cancer Pain *via* Immune and Neuronal Modulation. *Nat Commun* (2021) 12(1):4558. doi: 10.1038/s41467-021-24867-2

61. Liu Y, Jesus AA, Marrero B, Yang D, Ramsey SE, Sanchez GAM, et al. Activated STING in a Vascular and Pulmonary Syndrome. *N Engl J Med* (2014) 371(6):507–18. doi: 10.1056/NEJMoa1312625

62. Gorth DJ, Shapiro IM, Risbud MV. Transgenic Mice Overexpressing Human TNF-α Experience Early Onset Spontaneous Intervertebral Disc Herniation in the Absence of Overt Degeneration. *Cell Death Dis* (2018) 10(1):7. doi: 10.1038/s41419-018-1246-x

63. Kerr GJ, To B, White I, Millecamps M, Beier F, Grol MW, et al. Diet-Induced Obesity Leads to Behavioral Indicators of Pain Preceding Structural Joint Damage in Wild-Type Mice. *Arthritis Res Ther* (2021) 23(1):93. doi: 10.1186/s13075-021-02463-5

64. Rajan NE, Bloom O, Maidhof R, Stetson N, Sherry B, Levine M, et al. Toll-Like Receptor 4 (TLR4) Expression and Stimulation in a Model of Intervertebral Disc Inflammation and Degeneration. *Spine* (2013) 38(16):1343–51. doi: 10.1097/BRS.0b013e31826b71f4

65. Sun Z, Liu B, Luo Z-J. The Immune Privilege of the Intervertebral Disc: Implications for Intervertebral Disc Degeneration Treatment. *Int J Med Sci* (2020) 17(5):685–92. doi: 10.7150/ijms.42238

66. Adkisson HD, Milliman C, Zhang X, Mauch K, Maziarz RT, Streeter PR. Immune Evasion by Neocartilage-Derived Chondrocytes: Implications for Biologic Repair of Joint Articular Cartilage. *Stem Cell Res* (2010) 4(1):57–68. doi: 10.1016/j.scr.2009.09.004

67. Pereira RC, Martinelli D, Cancedda R, Gentili C, Poggi A. Human Articular Chondrocytes Regulate Immune Response by Affecting Directly T Cell Proliferation and Indirectly Inhibiting Monocyte Differentiation to Professional Antigen-Presenting Cells. *Front Immunol* (2016) 7:415. doi: 10.3389/fimmu.2016.00415

68. Torre OM, Mroz V, Bartelstein MK, Huang AH, Iatridis JC. Annulus Fibrosus Cell Phenotypes in Homeostasis and Injury: Implications for Regenerative Strategies. *Ann NY Acad Sci* (2019) 1442(1):61–78. doi: 10.1111/nyas.13964

69. Al-Asmari SS, Rajapakse A, Ullah TR, Pépin G, Croft LV, Gantier MP. Pharmacological Targeting of STING-Dependent IL-6 Production in Cancer Cells. *Front Cell Dev Biol* (2021) 9:709618. doi: 10.3389/fcell.2021.709618

70. de Hooge ASK, van de Loo FAJ, Bennink MB, Arntz OJ, de Hooge P, van den Berg WB. Male IL-6 Gene Knock Out Mice Developed More Advanced Osteoarthritis Upon Aging. *Osteoarthr Cartil* (2005) 13(1):66–73. doi: 10.1016/j.joca.2004.09.011

71. van de Loo FA, Kuiper S, van Enckevort FH, Arntz OJ, van den Berg WB. Interleukin-6 Reduces Cartilage Destruction During Experimental Arthritis. A Study in Interleukin-6-Deficient Mice. *Am J Pathol* (1997) 151(1):177–91.

72. Sundararaghavan V, Mazur MM, Evans B, Liu J, Ebraheim NA. Diabetes and Bone Health: Latest Evidence and Clinical Implications. *Ther Adv Musculoskelet Dis* (2017) 9(3):67–74. doi: 10.1177/1759720X16687480

Conflict of Interest: The authors declare that the research was conducted in the absence of any commercial or financial relationships that could be construed as a potential conflict of interest.

Publisher's Note: All claims expressed in this article are solely those of the authors and do not necessarily represent those of their affiliated organizations, or those of the publisher, the editors and the reviewers. Any product that may be evaluated in this article, or claim that may be made by its manufacturer, is not guaranteed or endorsed by the publisher.